PHYSICS

Observation of the magnonic Dicke superradiant phase transition

Dasom Kim[1,2,3]†, Sohail Dasgupta[4]†, Xiaoxuan Ma[5]†, Joong-Mok Park[3], Hao-Tian Wei[4], Xinwei Li[6], Liang Luo[3], Jacques Doumani[1,2], Wanting Yang[5], Di Cheng[3,7], Richard H. J. Kim[3], Henry O. Everitt[2,4,8,9], Shojiro Kimura[10], Hiroyuki Nojiri[10], Jigang Wang[3,7], Shixun Cao[5]*, Motoaki Bamba[11,12], Kaden R. A. Hazzard[4,8,13], Junichiro Kono[2,4,8,14]*

Two-level atoms ultrastrongly coupled with single-mode cavity photons are predicted to exhibit a quantum phase transition, entering a phase in which both the atomic polarization and the photonic field are finite even without external driving. However, this phenomenon, the superradiant phase transition (SRPT), is forbidden by a no-go theorem due to the existence of the diamagnetic term. Here, we present spectroscopic evidence for a magnonic SRPT in $ErFeO_3$, where the role of the photonic mode (two-level atoms) in the photonic SRPT is played by an Fe^{3+} magnon mode (Er^{3+} spins). The absence of the diamagnetic term in the Fe^{3+}-Er^{3+} exchange coupling ensures that the no-go theorem does not apply. Ultrabroadband terahertz and gigahertz magnetospectroscopy experiments revealed the signatures of the SRPT in thermal equilibrium, a kink and a softening, respectively, of two spin-magnon hybridized modes at the critical point. Systems near this phase are expected to harbor large-scale squeezing, which will potentially provide a route to next-generation quantum technologies.

INTRODUCTION

An ensemble of two-level atoms can exhibit coherence through cooperative interaction with a single-mode quantized radiation field. Such cooperative optical processes have been extensively studied since the pioneering work of Dicke (*1*) in the context of superradiance and have recently attracted much-renewed interest in cavity quantum electrodynamics (QED) (*2*–*4*), condensed matter physics (*5*–*7*), and quantum information science (*8*). While superradiance phenomena occur in excited or driven systems, recent cavity QED studies of materials have focused on thermal equilibrium modified by cavity-enhanced vacuum electromagnetic fields.

A profound consequence of the Dicke model is a quantum phase transition, superradiant phase transition (SRPT) (*9*, *10*), where when the strength of the cooperative light-matter coupling exceeds a critical value, a static coherent electric or magnetic field and a finite atomic polarization appear spontaneously and simultaneously. We use the term "quantum phase transition" to refer to a zero-temperature phase transition induced by changing a part of the Hamiltonian that does not commute with the rest of the Hamiltonian. Even at a finite temperature, while thermal fluctuations lead to classical critical scaling, intrinsically quantum phenomena persist. A marked example is the quantum squeezing (*11*) obtained near the SRPT not only at zero temperature but also at finite temperature.

Realization of the SRPT has been of much interest, but its occurrence in thermal equilibrium has been a subject of debate (*12*–*17*) due to the no-go theorem (*18*). Various methods have been proposed to circumvent the no-go theorem (*12*, *13*, *19*–*21*). At the core of the no-go theorem is the diamagnetic term (also known as the A^2 term, where A is the electromagnetic vector potential) that inevitably appears in the minimal-coupling Hamiltonian describing the electric-dipole photon-atom interaction (Fig. 1A, top); this term adds positive energy to the system, causing the ground state to be robust against the SRPT (*15*, *18*, *22*, *23*).

A recent theoretical study has suggested that a magnonic version of the SRPT can occur in $ErFeO_3$ via ultrastrong magnon-spin coupling because the nature of the coupling is spin-exchange interaction for which there is no A^2 term (*21*).

Further, terahertz (THz) magnetospectroscopy experiments on a crystal of $ErFeO_3$ have revealed ultrastrong coupling between a magnon mode of ordered Fe^{3+} spins and paramagnetic Er^{3+} spins (*24*). This system can be modeled by the Dicke model, where the Fe^{3+} magnon mode (the Er^{3+} spins) plays the role of the single cavity mode (the two-level atoms) of the Dicke model; see Fig. 1A (bottom). The Fe^{3+}-Er^{3+} coupling exhibits Dicke cooperativity (*1*, *5*), i.e., the Fe^{3+}-Er^{3+} coupling strength $\propto \sqrt{\rho}$, where ρ is the Er^{3+} spin density (*24*). More recently, a short-range atom-atom interaction (Er^{3+}-Er^{3+} exchange interaction) has been incorporated for the simulation of an extended Dicke model (*25*). However, spectroscopic signatures of the SRPT, i.e., a polariton frequency softening down to zero and a concomitant change in the other polariton branch, have not been achieved to date.

Here, we report an experimental demonstration of the magnonic SRPT in $ErFeO_3$ through magnetospectroscopy measurements in the THz and gigahertz (GHz) frequency ranges at low temperatures. We observed that, at the phase boundary between the superradiant (SR) phase and the normal (N) phase, the frequency of a branch of

[1]Applied Physics Graduate Program, Smalley–Curl Institute, Rice University, Houston, TX 77005, USA. [2]Department of Electrical and Computer Engineering, Rice University, Houston, TX 77005, USA. [3]Ames National Laboratory, Ames, IA 50011, USA. [4]Department of Physics and Astronomy, Rice University, Houston, TX 77005, USA. [5]Department of Physics, Materials Genome Institute, Institute for Quantum Science and Technology, Shanghai University, Shanghai 200444, China. [6]Department of Physics, National University of Singapore, Singapore 117551, Singapore. [7]Department of Physics and Astronomy, Iowa State University, Ames, IA 50011, USA. [8]Smalley–Curl Institute, Rice University, Houston, TX 77005, USA. [9]DEVCOM Army Research Laboratory-South, Houston, TX 77005, USA. [10]Institute for Materials Research, Tohoku University, Sendai 980-8577, Japan. [11]Department of Physics, Yokohama National University, Yokohama 240-8501, Japan. [12]Institute for Multidisciplinary Sciences, Yokohama National University, 79-5 Tokiwadai, Hodogaya-ku, Yokohama 240-8501, Kanagawa, Japan. [13]Department of Physics and Astronomy, University of California, Davis, CA 95616, USA. [14]Department of Materials Science and NanoEngineering, Rice University, Houston, TX 77005, USA.
*Corresponding author. Email: sxcao@shu.edu.cn (S.C.); kono@rice.edu (J.K.)
†These authors contributed equally to this work.

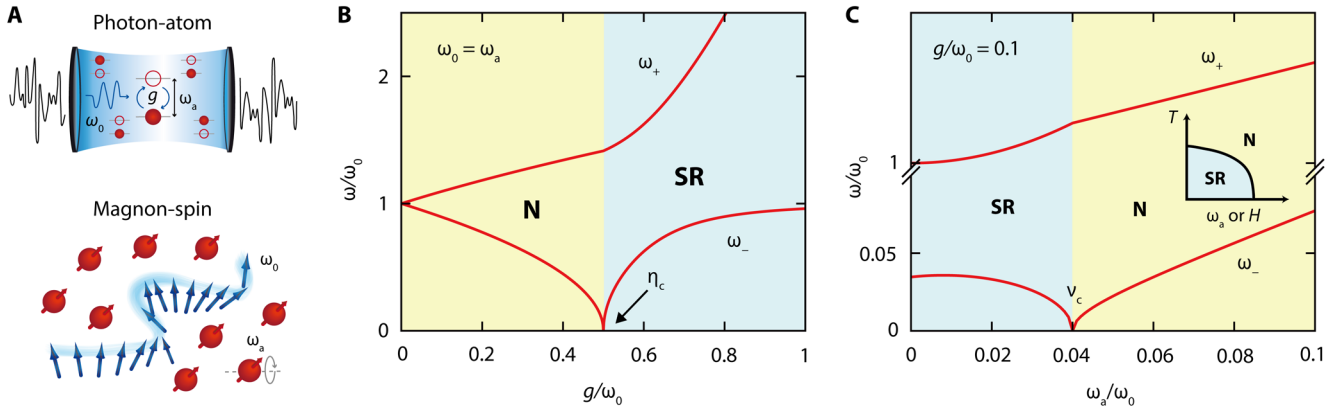

Fig. 1. Comparison between a light-matter system and a magnon-spin system for the Dicke SRPT. (**A**) Top: A light-matter hybrid system with coupling strength g realized in a single-mode cavity with frequency ω_0 containing an ensemble of two-level atoms with transition frequency ω_a. Bottom: A magnon-spin hybrid system realized in $ErFeO_3$. A single-mode magnon excitation of Fe^{3+} (an ensemble of Er^{3+} spins) plays the role of single-mode cavity photons (two-level atoms) in the Dicke model. (**B**) Normalized frequencies of the upper-polariton (ω_+) and lower-polariton (ω_-) modes as a function of g/ω_0 calculated using the simple Dicke model at zero-detuning ($\omega_0 = \omega_a$) in the thermodynamic limit. When ω_- reaches zero, an SRPT occurs between the normal (N) and superradiant (SR) phases. (**C**) Normalized frequencies of $\omega_\pm$ modes as a function of ω_a/ω_0 calculated using the simple Dicke model with $g/\omega_0 = 0.1$ in the thermodynamic limit. When the lower-polariton frequency reaches zero, the system crosses the SR-N phase boundary. The inset illustrates the SR-N phase boundary when ω_a/ω_0 is tuned by an external DC magnetic field H.

the Er^{3+} electron paramagnetic resonance (EPR) approaches zero while the frequency of an Fe^{3+} magnon displays a kink.

We developed an extended Dicke model, incorporating the single-ion anisotropy energy of Er^{3+} spins, which accurately reproduces the experimentally observed mode frequencies. The establishment of the magnonic SR phase will enable further experimental explorations of the nonintuitive vacuum-induced, squeezed ground states predicted for the SR phase (*26*–*28*) and of quantum information science (*29*) using magnonics (*30*, *31*). Our spectroscopic measurements are a key step in confirming the SRPT and understanding its nature before attempting entanglement measurements.

RESULTS

Expected spectroscopic signatures of the SRPT

The SRPT can be identified by the spectroscopic signatures of a simple Dicke model, describing a collection of N two-level atoms interacting with a single bosonic mode (*1*, *17*, *27*, *32*)

$$\hat{\mathcal{H}}^{(N)}/\hbar = \omega_0\hat{a}^\dagger\hat{a} + \omega_a\left(\hat{S}_z + \frac{N}{2}\right) + \frac{2g}{\sqrt{N}}\left(\hat{a}^\dagger + \hat{a}\right)\hat{S}_x \qquad (1)$$

where $\hat{a}^\dagger$ ($\hat{a}$) is a bosonic creation (annihilation) operator of frequency ω_0, ω_a is the transition frequency of the two-level atoms, $\hat{S}_i$ is a collective spin operator in the i direction, N is the number of two-level atoms, and g is the coupling strength between the bosonic mode and two-level atom. Later, we will derive a model similar to this from a spin Hamiltonian for a magnon-spin system containing extra terms that do not qualitatively change its eigenfrequencies and phase diagram. For a photon-atom system, one should also include proper diamagnetic or self-polarization terms to preserve the gauge invariance (*15*) and to recover the classical-quantum correspondence (*23*).

In the thermodynamic limit ($N \to \infty$), through the Holstein-Primakoff transformation (*27*, *32*), Eq. 1 becomes $\hat{\mathcal{H}}/\hbar = \omega_0\hat{a}^\dagger\hat{a} + \omega_a\hat{b}^\dagger\hat{b} + g\left(\hat{a}^\dagger + \hat{a}\right)\left(\hat{b}^\dagger + \hat{b}\right)$, where $\hat{b}^\dagger$ ($\hat{b}$) is a bosonic creation (annihilation) operator corresponding to the atomic excitations ω_a. Because this is a quadratic Hamiltonian, it can be analytically solved by a Bogoliubov transformation. Figure 1B plots the frequencies of the upper and lower polaritons, ω_+ and ω_-, respectively, normalized by ω_0 as a function of g/ω_0 at zero detuning, $\omega_0 = \omega_a$. The SRPT occurs, resulting in a complete frequency softening (a kink) of ω_- (ω_+) at the phase boundary. In this case, we can also derive a condition for the SRPT at zero temperature

$$g > \frac{\sqrt{\omega_a\omega_0}}{2} \qquad (2)$$

In the case of zero detuning ($\omega_a = \omega_0$), this condition reduces to $g > \omega_0/2$, i.e., $\eta_c = 0.5$ is the critical value for the normalized coupling strength $\eta \equiv g/\omega_0$. One can imagine that the effect of g is largest when the light and atom degrees of freedom are on-resonant at zero detuning. Therefore, the standard strategy for realizing the SRPT is to maximize g to reach $\eta_c = 0.5$ for a fixed ω_0 while maintaining zero detuning ($\omega_a = \omega_0$); see Fig. 1B. However, even when $\eta < 0.5$, the SRPT can occur if one can reduce ω_a to satisfy Eq. 2 for fixed g and ω_0. For example, when $\eta = 0.1$ (Fig. 1C), Eq. 2 becomes $\nu \equiv \omega_a/\omega_0 < 0.04$; that is, the SRPT occurs as a function of ν when it is decreased to the critical value $\nu_c = 0.04$. In general, when $\eta < 0.5$ ($\eta > 0.5$), the SRPT occurs at $\nu_c < 1$ ($\nu_c > 1$), i.e., on the left (right) side of the zero-detuning point when ω_a is varied for fixed g and ω_0; see section S1 and fig. S1 for details.

This nonstandard strategy aptly works for realizing a magnonic SRPT in $ErFeO_3$. The Fe^{3+}-Er^{3+} coupling strength g and the Fe^{3+} magnon frequency ω_0 are nearly independent of the applied magnetic field, H, and their ratio is $\eta < 1$, while the Er^{3+} EPR frequency ω_a strongly depends on the applied DC magnetic field, via the Zeeman effect. Therefore, applying a magnetic field can tune ν. With realistic values of g and ω_0 for $ErFeO_3$ (*21*, *25*, *33*), the SRPT is expected to occur at a critical magnetic field, H_c, when the temperature, T, is sufficiently low (inset to Fig. 1C). Notably, the critical temperature, T_c, is maximum when $\omega_a = 0$, i.e., when $H = 0$. As H increases, T_c decreases, and, hence, the SR phase is transformed into the N phase at

$H = H_c(T)$ when H is varied at a constant temperature; as T is decreased, H_c monotonically increases from zero to a maximum value at $T = 0$, which is a quantum critical point. Figure 1C shows the frequencies of the two polariton branches, $\omega_{\pm}$, normalized by ω_0, as a function of ν calculated using the simple Dicke model in the thermodynamic limit ($N \to \infty$) where we assumed $\eta = 0.1$, which is a typical value found in the ultrastrong coupling regime (*3*, *4*, *6*).

Magnetic structure of $ErFeO_3$

When 4 K < T < 87 K, Fe^{3+} spins are antiferromagnetically ordered along the *c* axis with a canting toward the *a* axis by a small angle β (Γ_2 in Bertaut's notation) induced by the Dzyaloshinskii-Moriya (DM) interaction, which produces a weak ferromagnetic moment along the *a* axis (*34*). Figure 2A (left) shows the orthorhombic perovskite structure of $ErFeO_3$ that consists of two Fe^{3+} and two Er^{3+} sublattices, described by the space group $D_{2h}^{16} - Pbnm$ with *a*, *b*, and *c* as the crystallographic axes that correspond to *x*, *y*, and *z* axes, respectively, in free space. As T decreases from 4 K, the Néel vector of Fe^{3+} spins continuously rotates toward the *b* axis (*35*), and paramagnetic Er^{3+} spins develop C-type antiferromagnetic order along the *c* axis (*36*) (Γ_{12} phase); see Fig. 2A (right). The definition of Γ phases is presented in table 1 of (*37*). A detailed description of its spin configuration in the Γ_{12} phase is presented in Fig. 2B. The two Fe^{3+} spins are denoted by $\hat{\mathbf{S}}^{\mathbf{A}}$ and $\hat{\mathbf{S}}^{\mathbf{B}}$, and the two Er^{3+} spins are denoted by $\hat{\mathfrak{s}}^{\mathbf{A}}$ and $\hat{\mathfrak{s}}^{\mathbf{B}}$. The plane where the Fe^{3+} spins exist has been rotated by θ = 49° with respect to the *ac* plane (*35*), while the Er^{3+} spins exist in the *ac* plane. M_{Fe} and M_{Er} are, respectively, defined as $\mathbf{S}^{\mathbf{A}} + \mathbf{S}^{\mathbf{B}}$ and $\mathfrak{s}^{\mathbf{A}} + \mathfrak{s}^{\mathbf{B}}$. Two order parameters for this phase transition can be defined as $\left\langle \hat{S}_y^{A/B} \right\rangle$ and $\left\langle \hat{\mathfrak{s}}_z^{A} - \hat{\mathfrak{s}}_z^{B} \right\rangle$, where $\hat{S}_y^{A/B}$ is the *y* component of the Fe^{3+} spins $\hat{\mathbf{S}}^{\mathbf{A/B}}$ and $\hat{\mathfrak{s}}_z^{A/B}$ is the *z* component of the Er^{3+} spins $\hat{\mathfrak{s}}^{\mathbf{A/B}}$. The former captures the rotation of the Fe^{3+} spins toward the *b* (*y*) axis, while the latter captures the antiferromagnetic ordering

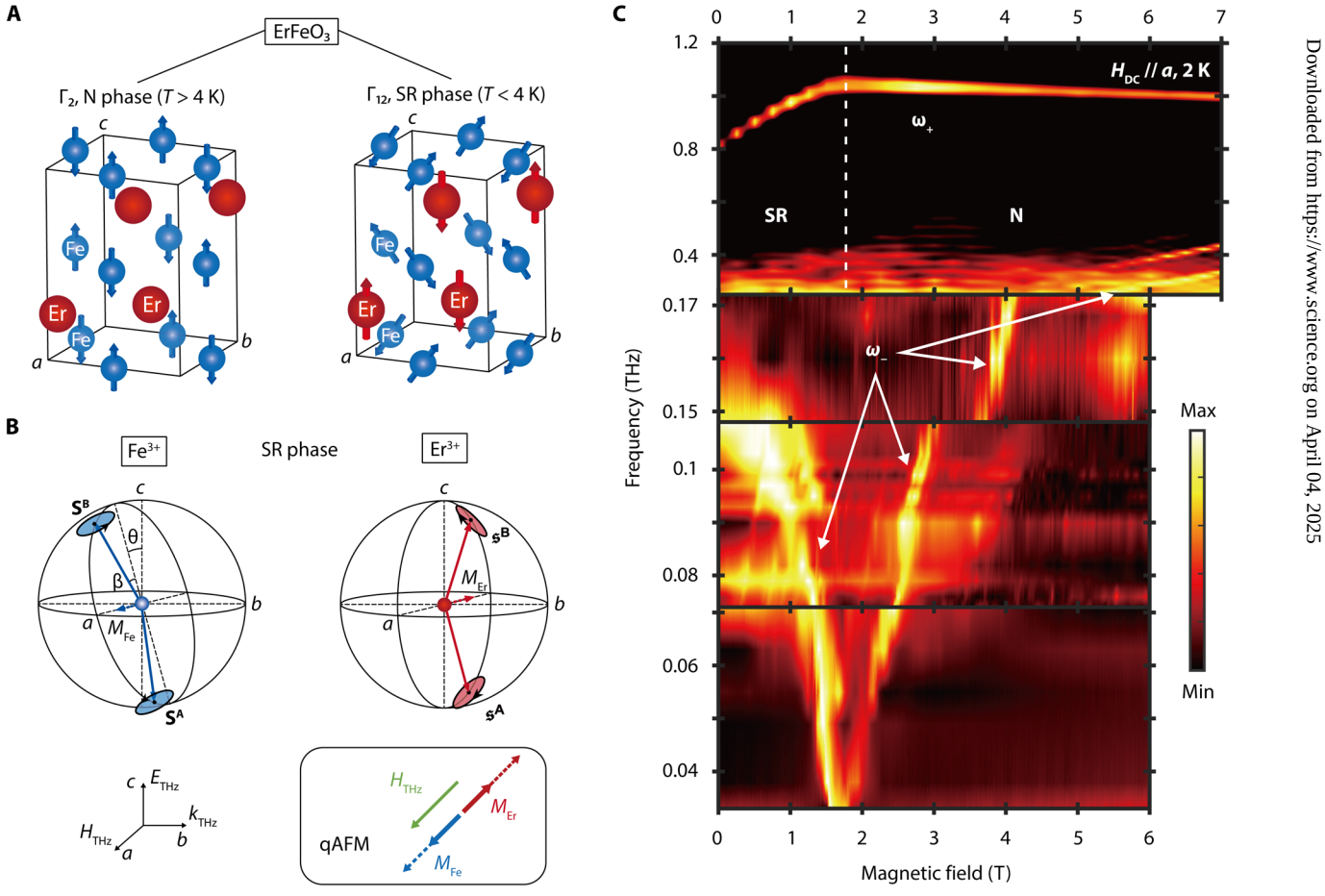

Fig. 2. Spectroscopic evidence for the magnonic SRPT in $ErFeO_3$. (**A**) Schematics of the magnetic structure of $ErFeO_3$ in the Γ_2 (N) phase and the Γ_{12} (SR) phase ($T < T_N^{Er} = 4$ K). Er^{3+} spins become antiferromagnetically aligned at low temperatures, while the Néel vector of the Fe^{3+} spins rotates toward the *b* axis. (**B**) Spin dynamics of the qAFM of Fe^{3+} spins and Er^{3+} spins in the Γ_{12} phase triggered by a THz magnetic field polarized along the *a* axis. The magnitude of the net magnetization (M_{Fe} and M_{Er}) oscillate (black box). The Fe^{3+} spins are ordered along the *c* axis and cant toward the *a* axis (β = 8.5 mrad). The plane where the Fe^{3+} spins lie is θ = 49° off from the *ac* plane. (**C**) Top: Transmission decrease ($1 - \tilde{T}$) as a function of magnetic field in THz time-domain magnetospectroscopy (THz-TDMS), showing a kink in the upper polariton. Here, the maximum (minimum) value is 1 (0.7). Two middle: Temperature spectra in the sample upon continuous-wave (CW) GHz illumination with a base temperature of 2 K. The maximum temperature change is less than 90 mK. Here all spectra are scaled from 0 to 1. Bottom: Negative transmission spectra. Here, all spectra are scaled from 0 to 1. The GHz spectra in the bottom three panels show a softening in the lower-polariton frequency, which together with the kink in the upper-polariton mode, demonstrates the magnonic SRPT; see Fig. 1C.

of the Er^{3+} spins along the c (z) axis. This phase transition ($\Gamma_2 \rightarrow \Gamma_{12}$) corresponds to the N → SR phase transition, i.e., the appearance of the static coherent electric or magnetic field and atomic polarizations in the context of a photonic SRPT (*21*). Below 4 K, the application of a magnetic field can induce a $\Gamma_{12} \rightarrow \Gamma_2$ transition (*38*, *39*), which we use in demonstrating the magnonic SRPT (SR → N).

THz and GHz magnetospectroscopy studies of $ErFeO_3$

We performed transmission magnetospectroscopy experiments on single crystals of $ErFeO_3$ (see Materials and Methods for sample preparation) in the Voigt geometry in the THz and GHz photon frequency ranges to monitor the magnetic field evolution of the $\omega_{\pm}$ modes of this Fe^{3+}-Er^{3+} hybrid system. The application of a static magnetic field, H_{DC}, along the a axis continuously tuned the "bare" Er^{3+} EPR frequency ω_a via the Zeeman effect, whereas the bare Fe^{3+} magnon mode frequency ω_0 was nearly independent of H_{DC}. Here, the bare frequencies refer to the frequencies of the Fe^{3+} and Er^{3+} modes when uncoupled. The magnetic field moved the system out of the SR phase into the N phase at a critical field of $\mu_0 H_{DC} = 1.8$ T at $T = 2$ K (where μ_0 is the vacuum permeability).

In the THz frequency range (frequencies above 0.25 THz), we used THz time-domain magnetospectroscopy (THz-TDMS) (*40*) to monitor the ω_+ mode; see Materials and Methods for experimental details. On the other hand, to monitor the ω_- mode in the GHz range, we used a set of continuous-wave (CW) devices (Virginia Diodes Inc.) producing single-frequency microwave radiation at frequencies below 172 GHz; see Materials and Methods for experimental details. From 33 to 71 GHz, we recorded the intensity of radiation transmitted through the sample as a function of magnetic field, which exhibited decreases at magnetic resonances. From 74 to 172 GHz, we monitored the sample temperature, which increased at resonance magnetic fields due to resonant absorption of microwave radiation; see fig. S8. Through these methods, we could locate the resonance frequencies of both the ω_+ and ω_- modes as a function of magnetic field.

In the THz-TDMS experiments, the magnetic field component of the incident THz wave was set to be parallel to the a axis to access the quasi-antiferromagnetic (qAFM) magnon mode of Fe^{3+} while a static magnetic field was applied along the a axis (*33*); see the black box in Fig. 2B. The THz magnetic field parallel to the net magnetization direction triggered the out-of-phase spin precession in $\mathbf{S}^{A/B}$ through the transient Zeeman torque, as shown in Fig. 2B. A b-cut sample made this configuration possible in the Voigt geometry. In this configuration, we found a pronounced absorption peak at 0.8 THz at 0 T, which we interpret as the ω_+ mode.

The top panel of Fig. 2C shows the magnetic field dependence of this mode in transmission decreases ($1 - \tilde{T}$), where $\tilde{T}$ is the transmittance. The data signal a clear phase transition at 1.8 T as a kink in the field evolution of its frequency. Below 1.8 T, frequency of the feature rapidly increased with H_{DC}, whereas above 1.8 T, it slowly decreased with increasing H_{DC}. This behavior is consistent with what is shown for the ω_+ mode in Fig. 1C.

The bottom three panels of Fig. 2C display spectra taken in the GHz range, showing a marked softening behavior of the ω_- mode. At 0 T, a broad feature is seen at around 150 GHz, but it rapidly sharpens and red shifts as the applied magnetic field increases. The frequency of this mode eventually becomes lower than the lower bound of our frequency range but quickly reappears with increasing field, leaving a field gap of 0.2 T between the two peaks at 33 GHz. The middle of these peaks is located at 1.8 T, which agrees with the kink position of the ω_+ mode in the top panel. This softening behavior is consistent with what is shown for the ω_- mode in Fig. 1C. A further increase of the field reveals a Zeeman-type response of the Er^{3+} spins, signifying the absence of antiferromagnetic order in the N phase. The ω_- mode eventually appears in THz absorption spectra in the top panel above 5.5 T, which confirms the consistency of our two different types of measurements. The less bright line that appears slightly above the ω_- mode does not play an important role in the SRPT (fig. S7).

Mean-field theory of the spin Hamiltonian

Because no exact solution exists for a Dicke model that includes atom-atom (Er^{3+}-Er^{3+} direct exchange) interaction, we model our experimental results with a spin Hamiltonian that has been widely studied for rare-earth orthoferrites (*21*, *41*, *42*), augmenting it with a term accounting for the anisotropy of the Er^{3+} spins. Then, we derived an extended Dicke model from the spin Hamiltonian to examine whether the A^2 term appears and to elucidate the role of the Fe^{3+} magnon mode and Er^{3+} EPR in the context of light-matter interaction.

The system can be described by a spin Hamiltonian on a bipartite lattice with a unit cell consisting of two Fe^{3+} and two Er^{3+} spins (*21*, *24*). Nearest-neighboring spins interact via direct magnetic exchange. Owing to strong spin-orbit coupling in Fe^{3+}, nearest neighbors of Fe^{3+} spins also have DM interactions between them. Both the Fe^{3+} and Er^{3+} spins are magnetically anisotropic, preferring the xz plane in our notation. Although the physical system has four Fe^{3+} spins and four Er^{3+} spins in a unit cell, the effective two-sublattice model can reproduce the resonance frequencies accurately because the Fe^{3+}-anisotropic energies are much smaller than the DM interaction energy (*34*, *41*). The spin Hamiltonian can be written as

$$\hat{\mathcal{H}}_{\text{spin}} = \hat{\mathcal{H}}_{\text{Fe}} + \hat{\mathcal{H}}_{\text{Er}} + \hat{\mathcal{H}}_{\text{Fe-Er}} \tag{3}$$

where

$$\begin{aligned}\hat{\mathcal{H}}_{\text{Fe}} = &\sum_{s=\text{A,B}}\sum_{i=1}^{N_0} \mu_0\mu_B \mathfrak{g}^x_{\text{Fe}} S^s_{i,x} H^{\text{DC}}_x + J_{\text{Fe}} \sum_{i,i'} \mathbf{S}^{\text{A}}_i \cdot \mathbf{S}^{\text{B}}_{i'} \\ &- D^y_{\text{Fe}} \sum_{i,i'} \left(S^{\text{A}}_{i,z} S^{\text{B}}_{i',x} - S^{\text{B}}_{i',z} S^{\text{A}}_{i,x}\right) \\ &- \sum_{s=\text{A,B}}\sum_{i=1}^{N_0} \left[A^x_{\text{Fe}} \left(S^s_{i,x}\right)^2 + A^z_{\text{Fe}} \left(S^s_{i,z}\right)^2\right],\end{aligned} \tag{4}$$

$$\begin{aligned}\hat{\mathcal{H}}_{\text{Er}} = &\sum_{s=\text{A,B}}\sum_{i=1}^{N_0} \mu_0\mu_B \mathfrak{g}^x_{\text{Er}} \mathfrak{s}^s_{i,x} H^{\text{DC}}_x + J_{\text{Er}} \sum_{i,i'} \mathfrak{s}^{\text{A}}_i \cdot \mathfrak{s}^{\text{B}}_{i'} \\ &- \sum_{s=\text{A,B}}\sum_{i=1}^{N_0} \left[A^x_{\text{Er}} \left(\mathfrak{s}^s_{i,x}\right)^2 + A^z_{\text{Er}} \left(\mathfrak{s}^s_{i,z}\right)^2\right],\end{aligned} \tag{5}$$

and

$$\hat{\mathcal{H}}_{\text{Fe-Er}} = \sum_{i=1}^{N_0} \sum_{s,s'=\text{A,B}} \left[J \mathfrak{s}^s_i \cdot \mathbf{S}^{s'}_i + \mathbf{D}^{s,s'} \cdot \left(\mathfrak{s}^s_i \times \mathbf{S}^{s'}_i\right)\right] \tag{6}$$

The $\mathbf{S}^{A/B}_i$ and $\mathfrak{s}^{A/B}_i$ correspond to Fe^{3+} ($S = 5/2$) and Er^{3+} ($\mathfrak{s} = 1/2$) spin operators at the ith site in the A/B sublattice; $\sum_{i,i'}$ represents a

sum over the appropriate nearest neighbors; J_{Er}, J_{Fe}, and J are the direct exchange coupling strengths between Er^{3+}-Er^{3+}, Fe^{3+}-Fe^{3+}, and Fe^{3+}-Er^{3+} spins, respectively; D^{y}_{Fe} and $\mathbf{D}^{s,s'}$ are the DM interaction strength between Fe^{3+}-Fe^{3+} and Fe^{3+}-Er^{3+} spins, respectively; $A^{x/z}_{Fe}$ and $A^{x/z}_{Er}$ are the anisotropy strengths of Fe^{3+} and Er^{3+} spins, respectively, along the x/z axes; $\mathfrak{g}^{x}_{Fe/Er}$ are the x component of the Landé g-factor tensors for Fe^{3+} and Er^{3+} spins, which are assumed to be diagonal; μ_B is the Bohr magneton. We included Er^{3+}-anisotropy terms in Eq. 5, which were neglected in previous studies (*21*, *24*). Consistent with the inclusion of this term, magnetization measurements (*43*, *44*) suggest that Er^{3+} anisotropy is strong in this material. The inclusion of the terms is further necessitated by its large value compared to the exchange interaction between the Er^{3+} spins, i.e., $A^{x/z}_{Er} > J_{Er}$. Including the Er^{3+}-anisotropy terms in the Hamiltonian produces a noticeably improved fit to the experimental data.

We note that, according to recent neutron scattering experiments performed on $ErFeO_3$ below 4 K, the dispersion of the Er^{3+} spin excitation is found to be surprisingly weak even below 4 K (*36*).

Figure 3A displays a mean-field T-H phase diagram of the spin Hamiltonian, for $0 \le T \le 6$ K and $0 \le \mu_0 H \le 3$ T. This phase diagram, consistent with (*38*), shows the SR-phase boundary obtained by using $\left\langle \hat{\mathfrak{s}}^{A}_{z} - \hat{\mathfrak{s}}^{B}_{z} \right\rangle$ of Er^{3+} spins as the order parameter. One can also use $\left\langle \hat{S}^{A/B}_{y} \right\rangle$ of Fe^{3+} to construct the same phase boundary, because the two subsystems simultaneously order (fig. S11). The spin configurations are shown as an inset in Fig. 3A. The order parameters are obtained by performing a mean-field calculation on Eq. 3. The finite-temperature average of the spin operators then gives the self-consistency equations

$$\left\langle \mathfrak{s}^{s}_{\parallel} \right\rangle = -\frac{1}{2}\tanh\left(\frac{\mathfrak{g}_{Er}\mu_B \left| \overline{\mathbf{B}}^{s}_{Er} \right|}{2k_B T} \right) \tag{7}$$

$$\left\langle S^{s}_{\parallel} \right\rangle = -B_S\left(\frac{S\mathfrak{g}_{Fe}\mu_B \left| \overline{\mathbf{B}}^{s}_{Fe} \right|}{k_B T} \right) \tag{8}$$

where $B_S(x) = \frac{2S+1}{2S}\coth\left(\frac{2S+1}{2S}x\right) - \frac{1}{2S}\coth\left(\frac{x}{2S}\right)$ is the Brillouin function and k_B the Boltzmann constant. $\mathbf{B}^{s}_{Er}$ ($\mathbf{B}^{s}_{Fe}$) are mean fields for the Er^{3+} (Fe^{3+}) spins with $s \in \{A, B\}$ with the assumption that spins are spatially uniform; see Eqs. 14 and 15.

Above 4 K at 0 T, the Fe^{3+} spins are antiferromagnetically ordered, while Er^{3+} spins are paramagnetic (Fig. 2A). As we cool down the system, the b-axis component of Fe^{3+} spins becomes finite through the rotation of the Néel vector around the a axis. This rotation behavior has been evidenced by nuclear magnetic resonance experiments (*35*). At the same time, Er^{3+} spins antiferromagnetically order along the c axis (Fig. 2A). When we apply an external magnetic field along the a axis stronger than H_c, we break the antiferromagnetic ordering of Er^{3+} spins and restore the Fe^{3+} Néel vector along the c axis. These occur simultaneously due to the Fe^{3+}-Er^{3+} antisymmetric exchange interaction that couples spins and magnons in the Dicke model as we discuss in the following.

Figure 3B shows the frequencies of both polariton branches, calculated on the basis of the spin Hamiltonian, below (2 K, left) and above (10 K, right) the critical temperature as a function of H_{DC}, together with experimental results from Fig. 2C and fig. S6B. For the high-temperature measurements, see section S2. The calculated results are obtained by the linearized Heisenberg equations of motion

$$\hbar\frac{d}{dt}\delta\mathfrak{s}^{s} = -\delta\mathfrak{s}^{s}\times\mathfrak{g}_{Er}\mu_B\overline{\mathbf{B}}^{s}_{Er}\left(\mathfrak{s}^{A/B}, \mathbf{S}^{A/B}\right) - \overline{\mathfrak{s}}^{s}\times\mathfrak{g}_{Er}\mu_B\mathbf{B}^{s}_{Er}\left(\delta\mathfrak{s}^{A/B}, \delta\mathbf{S}^{A/B}\right) \tag{9}$$

$$\hbar\frac{d}{dt}\delta\mathbf{S}^{s} = -\delta\mathbf{S}^{s}\times\mathfrak{g}_{Fe}\mu_B\overline{\mathbf{B}}^{s}_{Er}\left(\mathfrak{s}^{A/B}, \mathbf{S}^{A/B}\right) - \overline{\mathbf{S}}^{s}\times\mathfrak{g}_{Fe}\mu_B\mathbf{B}^{s}_{Er}\left(\delta\mathfrak{s}^{A/B}, \delta\mathbf{S}^{A/B}\right) \tag{10}$$

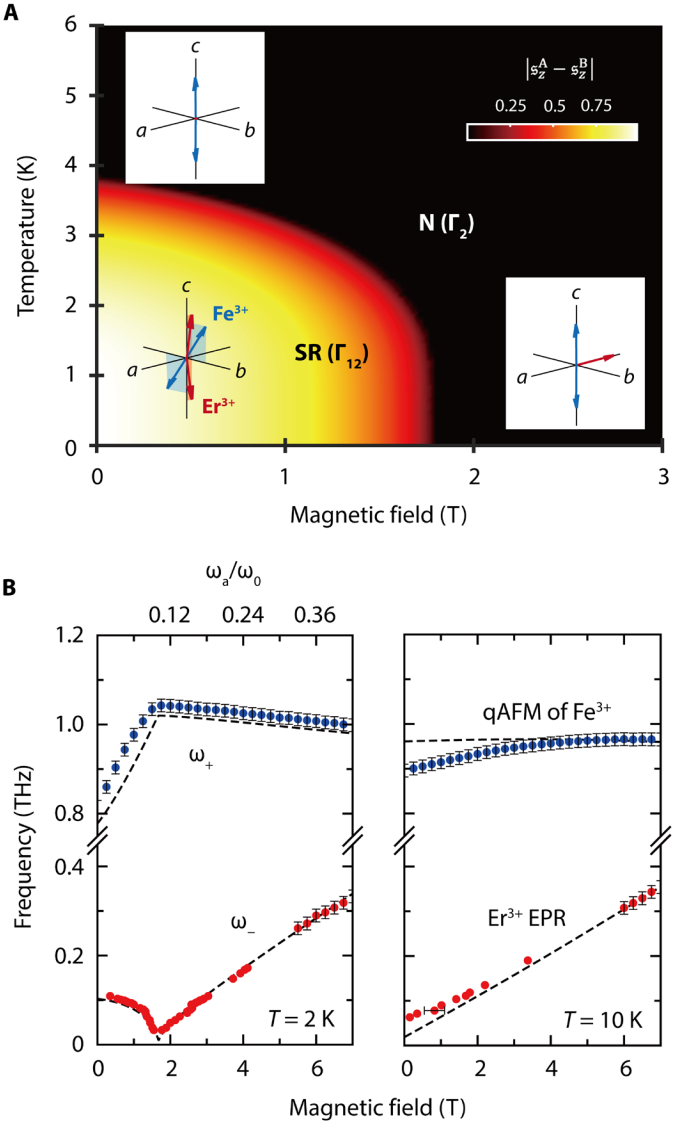

Fig. 3. Mean-field calculation for the spin Hamiltonian of $ErFeO_3$ in $\vec{H}_{DC} \parallel a$. (**A**) Theoretical T-H phase diagram. Insets: Schematics of the spin configuration in each phase. (**B**) Resonance frequencies of each spin subsystem as a function of the external magnetic field at 2 K (left) and 10 K (right). Dots, experimental results; dashed lines, calculated resonance frequencies. The top x axis on the left panel shows the SRPT occurs at the ratio of $\omega_a/\omega_0 = 0.11$. The vertical error bars indicate a frequency resolution determined by the time window ($\Delta f = 1/33$ ps $= 0.0286$ THz). The horizontal error bar indicates an SD.

where $\delta\mathfrak{s}^s$ and $\delta\mathbf{S}^s$ are the difference between the spin operators and their mean-field values. Then, resonance frequencies of Er^{3+} and Fe^{3+} spins are obtained by $\delta\mathfrak{s}^s = \mathfrak{s}^s(0)e^{i\omega^s_{Er}t}$ and $\delta\mathbf{S}^s = \delta\mathbf{S}^s(0)e^{i\omega^s_{Fe}t}$. A more detailed description is provided in Materials and Methods.

At 2 K, a good agreement was obtained by adjusting parameters in Eq. 3; see Materials and Methods, and table S1 for fitting. In particular, our calculations reproduced the observed ω_+ kink and ω_- softening. At 10 K, we calculated the frequencies with the parameters obtained at 2 K. The two modes at 10 K do not display any critical behavior and are much less hybridized. Therefore, the two branches are essentially the qAFM mode of Fe^{3+} spins ($\sim\omega_0$) and the EPR of Er^{3+} spins ($\sim\omega_a$), respectively.

Note that the zero-field value of the Er^{3+} resonance is finite even at 10 K. This zero-field splitting is a result of the lifted degeneracy of the Er^{3+} ground state doublets (*24*, *45*) due to the symmetric Fe^{3+}-Er^{3+} exchange interaction that exerts an internal effective magnetic field on Er^{3+} spins. Our fitting extracts the bare ω_0 and ω_a appearing in the extended Dicke model, and, using these values, we indicate the value of $\nu = \omega_a/\omega_0$ in the top x axis in the left panel, finding the critical ratio $\nu_c \sim 0.11$.

Derivation of the extended Dicke model

We derived the extended Dicke model from the spin Hamiltonian, which manifests the role of the bare qAFM mode of Fe^{3+} (ω_0) and bare Er^{3+} EPR (ω_a) and the cooperative nature of coupling between the two modes, where no A^2 term appears $\left[A \propto \left(\hat{a}^\dagger + \hat{a}\right)\right]$; see Materials and Methods for details. To derive the extended Dicke model, we first rewrite the Fe^{3+} subsystem $\hat{\mathcal{H}}_{Fe}$ in terms of magnon annihilation and creation operators. Next, we apply the collective spin approximation on the Er^{3+} subsystem $\hat{\mathcal{H}}_{Er}$. Last, we rewrite $\hat{\mathcal{H}}_{Fe-Er}$ in terms of the spin-fluctuation operators of the Fe^{3+} spins and the collective spin operators of Er^{3+} spins. As a result, we end up having a Dicke-type Hamiltonian, which we call the extended Dicke model. In the model, we find the following three terms that compose the simple Dicke model

$$\frac{\hat{\mathcal{H}}_{\text{Dicke}}}{\hbar} \sim \omega_0\hat{a}^\dagger\hat{a} + \omega_a\hat{\Sigma}^+_x + \frac{ig_z}{\sqrt{N_0}}\left(\hat{a}^\dagger - \hat{a}\right)\hat{\Sigma}^-_z + \dots \qquad (11)$$

where $\hat{a}^\dagger$ ($\hat{a}$) is a qAFM magnon creation (annihilation) operator, $\omega_a = \mu_0\mu_B\mathfrak{g}^x_{Er}H^{DC}_x/\hbar$, $\hat{\Sigma}^{A/B}_\xi = \sum_{i=1}^{N_0}\hat{\mathfrak{s}}^{A/B}_{i,\xi}$ is a collective spin operator, $\hat{\Sigma}^\pm_\xi = \hat{\Sigma}^A_\xi \pm \hat{\Sigma}^B_\xi$, and N_0 is the number of unit cells. The Σ^- (Σ^+) mode corresponds to the out-of-phase (in-phase) precession of Er^{3+} spins in the two sublattices. The additional terms in the extended Dicke model modifying the simple Dicke model are presented in Materials and Methods; see Eq. 39.

This model resembles the simple Dicke model in Eq. 1, which lacks the A^2 term, and, therefore, the no-go theorem does not apply (*18*). H^{DC}_x provides the tunability on the two-level transition energy through ω_a. The third term captures the Dicke cooperative interaction through N_0. We proved that g_z is the dominant contribution for the SRPT over other terms not shown here, in section S4. The form of g_z is provided in Eq. 43, and the origin of g_z essentially stems from the x component of the DM interaction between Fe^{3+} and Er^{3+} spins (*21*), i.e., the coupling between the two order parameters $\left\langle\hat{S}^{A/B}_y\right\rangle$ and $\left\langle\hat{\mathfrak{s}}^A_z - \hat{\mathfrak{s}}^B_z\right\rangle$. Together with the previous observation of the Dicke cooperativity (the coupling strength $\propto\sqrt{\rho}$) (*24*) and of hybridization of Fe^{3+} qAFM and the lower Er^{3+} EPR mode (see section S3), this direct correspondence concludes that our observation of the simultaneous kink and softening in $ErFeO_3$ is the evidence of the SRPT. We note that the model is in the linear regime and vacuum regardless of the application of the magnetic field and is free from the gauge principle because the coupling stems from magnon-spin interactions, instead of photon-atom interactions where the gauge principle is important.

DISCUSSION

We provided spectroscopic evidence that the $\Gamma_{12} \rightarrow \Gamma_2$ phase transition in $ErFeO_3$ can be understood as the SR → N transition central to quantum optics (*21*). The simultaneous observation of the kink and softening of polariton branches at the same critical point is crucial for demonstrating the hybridization of the degrees of freedom and occurrence of the magnonic SRPT. This phase transition can also be regarded as the magnetic transition of the Jahn-Teller type (*46*, *47*). What makes our mode softening distinct from others found in various solids is the concomitant kink and applicability of the Dicke model. While our softening resembles a softening at a spin-flop transition (SFT), as found in MnF_2 (easy-axis antiferromagnet) (*48*), the softening occurs without any concomitant kink because only one magnetic sublattice exists in the material. Furthermore, this softening occurs only when the external magnetic field is applied parallel to the Nèel vector (easy axis), in contrast to our work where the field is applied perpendicular to the Nèel vector (hard axis). Last, an SFT is typically a first-order phase transition that exhibits a discontinuous change, or a jump, in magnetization and may be accompanied by phase coexistence and hysteresis. On the other hand, the magnonic SRPT is a second-order phase transition where a continuous change occurs in magnetization. The $\Gamma_{12} \rightarrow \Gamma_2$ phase transition is a second-order phase transition where no discontinuous change is observed in magnetization measurements (*49*). Furthermore, an SFT occurs when a magnetic field (H_{DC}) is applied parallel to the Néel vector. In this work, all measurements were performed with $\vec{H}_{DC} \parallel a$, meaning that H_{DC} was always applied perpendicular to the Néel vector of Er^{3+} spins (c axis), so an SFT was not a possibility. In conclusion, our softening does not stem from a simple SFT.

Our work is readily applied to other solids, such as other rare-earth orthoferrite or orthochromite compounds, where two different magnetic sublattices strongly interact with each other, which host different types of phase transitions (*50*–*52*). One can simulate different types of Dicke models or explore novel quantum vacuum phenomena at or in the SR phase by judiciously choosing candidate materials. We suggest two necessary conditions that must be satisfied for this analogy to be valid as a general guidance. First, one should find evidence that g exhibits the Dicke cooperative enhancement. Second, at the SR-phase boundary, one should find a simultaneous change in two magnetic sublattices that can be revealed by a kink and softening in spectroscopic measurements. Theoretical mapping of a spin Hamiltonian into Dicke models should be possible.

In conclusion, we observed the spectroscopic signatures of the magnonic SRPT in $ErFeO_3$ in thermal equilibrium. Our work demonstrates the long-sought SRPT predicted by Hepp and Lieb in the Dicke model without the A^2 term (*9*). The magnon-spin system opens up the possibilities to explore novel quantum vacuum phenomena

predicted in the SR phase. At the SR-phase boundary of the Dicke model, a two-mode ground state becomes perfectly squeezed (*27*). This suggests that $ErFeO_3$ in a magnetic field offers a unique opportunity to achieve large-scale quantum entanglement essential for quantum information science. Furthermore, our work provides insights into achieving photonic SRPTs through an exchange pathway with a readily achievable coupling strength in recent cavity QED, as well as a way to discover and control condensed matter phases based on powerful concepts developed in QED.

MATERIALS AND METHODS

Sample preparation

Polycrystalline $ErFeO_3$ was first synthesized by a conventional solid-state reaction method using Er_2O_3 (99.9%) and Fe_2O_3 (99.98%) powders. According to the stoichiometric ratio, the original reagents were weighed carefully and pulverized with moderate anhydrous ethanol in an agate mortar. Mixtures were sintered at 1300°C for 1000 min and then cooled to room temperature. The sintered powders were thoroughly reground and pressed into a rod that was 70 mm in length and 6 mm in diameter by a Hydrostatic Press System (Riken Seiki Co. Ltd., model HP-M-SD-200) at 70 MPa and then sintered again at 1300°C for sufficient reaction. Single-crystal samples were then grown by an optical floating zone furnace (FZT-10000-H-VI-P-SH, Crystal Systems Corp; heat source: four 1-kW halogen lamps). Conditions like the melting power and the rate of sample rotation were stabilized and controlled in the molten zone.

THz time-domain magnetospectroscopy

We performed THz-TDMS measurements in the Voigt geometry as we described in the "THz and GHz magnetospectroscopy studies of $ErFeO_3$" section. A *b*-cut sample (1162 μm thick) was placed in a dry magneto-optical cryostat (Quantum Design, OptiCool) with variable temperatures T between 2 and 300 K and static magnetic fields $\mu_0 H$ up to 7 T. We generated THz pulses via optical rectification using a Ti:sapphire amplifier (795 nm, 40 fs, 1 kHz, Spectra-Physics, Spitfire Ace Pro XP) as a laser source that pumps a 1-mm-thick (110) zinc telluride (ZnTe) crystal, while detection was accomplished through electro-optical sampling in another ZnTe crystal with the same thickness.

Thermal detection of EPR modes in static magnetic fields under GHz irradiation

We performed GHz magnetospectroscopy measurements in the Voigt geometry, as we described in the "THz and GHz magnetospectroscopy studies of ErFeO" section. Figure S8A shows the setup used for thermal detection of Er^{3+} EPR modes. We generated CW GHz waves using a diode (70 to 110 GHz, 25 mW, Virginia Diode, WR10SGX). For the frequency range of 140 to 220 GHz, a frequency multiplier (3.2 mW, WR5.1x2) was added. A 90 off-axis parabolic mirror collimated the GHz radiation beam that was incident onto the sample to ensure that the whole area of the sample (4 mm in diameter) was uniformly illuminated. A wire-grid polarizer defined the GHz magnetic field polarization direction to be along the *a* axis. A *c*-cut sample (800 μm thick) was placed in a dry magneto-optical cryostat (Quantum Design, OptiCool) at 2 K and static magnetic fields $\mu_0 \vec{H}_{DC} \parallel a$ up to 6 T. A temperature sensor was located about 5 mm away from the sample, and they sat on the same copper plate. Temperature fluctuations of 1 mK or less were obtained with the temperature sensor (Lake Shore, CX-1050-CU-HT-1.4 M), and sensitivity of it is $dR/dT = -1120.8$ ohms K^{-1}. We swept the magnetic field for each fixed frequency to 6 T with a step size of 0.02 T. At each magnetic field, we waited 5 s for the temperature to stabilize. We selected frequencies that showed a temperature change of 30 mK $< \Delta T <$ 90 mK at the peak temperature.

Figure S8B shows an example of thermal detection. With 90-GHz illumination, the sample temperature increased at some magnetic fields as we increased the magnetic field. This is because when the incident photon energy coincides with the transition energy of the spin resonances, nonradiative electron relaxation emitting phonons can happen, thereby increasing the lattice temperature. This technique has been used for observing electron cyclotron resonance in electron gases in semiconductors in the microwave regime (*53*). One of the advantages of using this method over the transmission measurement is that one can avoid the notorious standing wave effects that make the transmission curve more complicated.

Figure S9A shows experimental data at 2 K obtained through this method with frequencies ranging from 74 to 172 GHz, which are 0-to-1 scaled. These data correspond to those shown in the middle two panels in Fig. 2C. Above 95 GHz, side peaks appear at around 1.5 T. They are hybridized modes of the Er^{3+} EPR and a Fabry-Pérot cavity mode defined by the thickness of the crystal (*54*). For measurements at 10 K, this method does not work because the cryostat can maintain the temperature at 10 K even with GHz radiation. At 2 K, however, the cryostat is using its maximum cooling capability, and thereby any additional thermal load increases the temperature.

GHz transmission spectroscopy experiments in pulsed magnetic fields

EPR measurements in pulsed magnetic fields with fixed frequencies ranging from 33 to 71 GHz and from 63 to 190 GHz were performed at temperatures of 2 and 10 K, respectively. Pulsed magnetic fields up to 6 T were applied parallel to the *a* axis. All curves have been 0-to-1 scaled.

At 2 K, we were able to observe the resonances as dips in transmission because the sample used for the pulsed magnetic field experiments was thinner ($d = 200$ μm) than the incident wavelengths (~1 cm), allowing us to avoid the standing waves effect inside the sample (fig. S9A). Note that the dielectric constant of $ErFeO_3$ is about 30. These data correspond to those shown in the bottom panel in Fig. 2C. Figure S9B shows transmission spectra at 10 K. These data are used in Fig. 3B (right). Here, because the thermal energy of 10 K (208 GHz) is higher than the transition energies, the population in the upper level is high, and, thereby, the transmission changes are minute. This results in high background noise at low frequencies after we do the 0-to-1 scale.

Mean-field calculation of resonance frequencies and a phase diagram from the spin Hamiltonian

We calculated the $\omega_{\pm}$ by a combination of mean-field theory and linearization of the Heisenberg equations of motion of the spin operators, as in (*21*). Assuming that the average values of the spin operators, $\mathbf{S}^{A/B}$ and $\mathfrak{s}^{A/B}$, are the same in all the unit cells, we self-consistently solved for the 12 mean fields, $\overline{\mathbf{S}}^{A/B}$ and $\overline{\mathfrak{s}}^{A/B}$ in thermal equilibrium. The resonance frequency was obtained by linearizing the Heisenberg equations of motion of these 12 spin operators around the mean-field values and solving the resulting linear differential equations.

We calculate the resonance frequencies from the spin Hamiltonian with the method of (*21*). The Heisenberg equations of motion of the 12 spin operators are

$$\hbar\frac{d\hat{\mathfrak{s}}^s}{dt} = -\hat{\mathfrak{s}}^s \times \mathfrak{g}_{\mathrm{Er}}\mu_{\mathrm{B}}\mathbf{B}^s_{\mathrm{Er}}\left(\hat{\mathfrak{s}}^{\mathrm{A/B}}, \mathbf{S}^{\mathrm{A/B}}\right) \tag{12}$$

$$\hbar\frac{d\mathbf{S}^s}{dt} = -\mathbf{S}^s \times \mathfrak{g}_{\mathrm{Fe}}\mu_{\mathrm{B}}\mathbf{B}^s_{\mathrm{Fe}}\left(\hat{\mathfrak{s}}^{\mathrm{A/B}}, \mathbf{S}^{\mathrm{A/B}}\right) \tag{13}$$

dropping the unit cell index due to the assumption that spins are spatially uniform, with $s \in \{\mathrm{A}, \mathrm{B}\}$, and $\mathbf{B}^s_{\mathrm{Er}}$ ($\mathbf{B}^s_{\mathrm{Fe}}$) the mean fields for the Er^{3+} (Fe^{3+}) spins

$$\mathbf{B}^s_{\mathrm{Er}} = \mathbf{B}^{\mathrm{DC}} + \frac{2z_{\mathrm{Er}}J_{\mathrm{Er}}}{\mu_{\mathrm{B}}\mathfrak{g}_{\mathrm{Er}}}\hat{\mathfrak{s}}^{\bar{s}} + \frac{2}{\mu_{\mathrm{B}}\mathfrak{g}_{\mathrm{Er}}}\sum_{s'=\mathrm{A,B}}\left[J\mathbf{S}^s - \left(\mathbf{D}^{s,s'}\times\mathbf{S}^s\right) - \mathbf{A}_{\mathrm{Er}}\cdot\hat{\mathfrak{s}}^s\right] \tag{14}$$

$$\mathbf{B}^s_{\mathrm{Fe}} = \mathbf{B}^{\mathrm{DC}} + \frac{2z_{\mathrm{Fe}}J_{\mathrm{Fe}}}{\mu_{\mathrm{B}}\mathfrak{g}_{\mathrm{Fe}}}\mathbf{S}^{\bar{s}} - \frac{z_{\mathrm{Fe}}}{\mu_{\mathrm{B}}\mathfrak{g}_{\mathrm{Fe}}}\mathbf{D}_{\mathrm{Fe}}\times\mathbf{S}^{\bar{s}} + \frac{2}{\mu_{\mathrm{B}}\mathfrak{g}_{\mathrm{Fe}}}\sum_{s'=\mathrm{A,B}}\left[J\mathbf{S}^s - \left(\mathbf{D}^{s,s'}\times\mathbf{S}^s\right) - \mathbf{A}_{\mathrm{Fe}}\cdot\hat{\mathfrak{s}}^s\right] \tag{15}$$

where $\bar{s}$ is the complementary sublattice of s and $z_{\mathrm{Fe}} = 6$ is the number of nearest neighboring Fe^{3+} spins. $\mathbf{D}^{s,s'}$ are expressed in terms of two values D_x and D_y as $\mathbf{D}^{\mathrm{A,A}} = \left(D_x, D_y, 0\right)^{\mathrm{t}}$, $\mathbf{D}^{\mathrm{A,B}} = \left(-D_x, -D_y, 0\right)^{\mathrm{t}}$, $\mathbf{D}^{\mathrm{B,A}} = \left(-D_x, D_y, 0\right)^{\mathrm{t}}$, and $\mathbf{D}^{\mathrm{B,B}} = \left(D_x, -D_y, 0\right)^{\mathrm{t}}$. Equation 15 is the same as that in (*21*), but Eq. 14 has an additional term coming from the inclusion of the Er^{3+} anisotropy.

The equations of motion are linearized around the equilibrium mean fields, $\overline{\mathbf{B}}^s_{\mathrm{Er/Fe}} \equiv \mathbf{B}_{\mathrm{Er/Fe}}\left(\overline{\hat{\mathfrak{s}}}^{\mathrm{A/B}}, \overline{\mathbf{S}}^{\mathrm{A/B}}\right)$. These equations of motion correspond to the effective Hamiltonians for the Er^{3+} and Fe^{3+} spins

$$\mathcal{H}^s_{\mathrm{Er}} = \mathfrak{g}_{\mathrm{Er}}\mu_{\mathrm{B}}\hat{\mathfrak{s}}^s \cdot \overline{\mathbf{B}}^s_{\mathrm{Er}} = \mathfrak{g}_{\mathrm{Er}}\mu_{\mathrm{B}}\hat{\mathfrak{s}}^s_{\parallel}\left|\overline{\mathbf{B}}^s_{\mathrm{Er}}\right| \tag{16}$$

$$\mathcal{H}^s_{\mathrm{Fe}} = \mathfrak{g}_{\mathrm{Fe}}\mu_{\mathrm{B}}\mathbf{S}^s \cdot \overline{\mathbf{B}}^s_{\mathrm{Fe}} = \mathfrak{g}_{\mathrm{Fe}}\mu_{\mathrm{B}}\mathbf{S}^s_{\parallel}\left|\overline{\mathbf{B}}^s_{\mathrm{Fe}}\right| \tag{17}$$

where $\hat{\mathfrak{s}}_{\parallel}$ ($\mathbf{S}_{\parallel}$) is the spin operator in the direction parallel to the mean field.

The finite-temperature average of the spin operators then gives the self-consistency equations

$$\left\langle \hat{\mathfrak{s}}^s_{\parallel} \right\rangle = -\frac{1}{2}\tanh\left(\frac{\mathfrak{g}_{\mathrm{Er}}\mu_{\mathrm{B}}\left|\overline{\mathbf{B}}^s_{\mathrm{Er}}\right|}{2k_{\mathrm{B}}T}\right) \tag{18}$$

$$\left\langle S^s_{\parallel} \right\rangle = -B_S\left(\frac{S\mathfrak{g}_{\mathrm{Fe}}\mu_{\mathrm{B}}\left|\overline{\mathbf{B}}^s_{\mathrm{Fe}}\right|}{k_{\mathrm{B}}T}\right) \tag{19}$$

where $B_S(x) = \frac{2S+1}{2S}\coth\left(\frac{2S+1}{2S}x\right) - \frac{1}{2S}\coth\left(\frac{x}{2S}\right)$ is the Brillouin function.

The linearized equations of motion are thus found to be

$$\hbar\frac{d}{dt}\delta\hat{\mathfrak{s}}^s = -\delta\hat{\mathfrak{s}}^s \times \mathfrak{g}_{\mathrm{Er}}\mu_{\mathrm{B}}\overline{\mathbf{B}}^s_{\mathrm{Er}}\left(\hat{\mathfrak{s}}^{\mathrm{A/B}}, \mathbf{S}^{\mathrm{A/B}}\right) - \overline{\hat{\mathfrak{s}}}^s \times \mathfrak{g}_{\mathrm{Er}}\mu_{\mathrm{B}}\mathbf{B}^s_{\mathrm{Er}}\left(\delta\hat{\mathfrak{s}}^{\mathrm{A/B}}, \delta\mathbf{S}^{\mathrm{A/B}}\right) \tag{20}$$

$$\hbar\frac{d}{dt}\delta\mathbf{S}^s = -\delta\mathbf{S}^s \times \mathfrak{g}_{\mathrm{Fe}}\mu_{\mathrm{B}}\overline{\mathbf{B}}^s_{\mathrm{Er}}\left(\hat{\mathfrak{s}}^{\mathrm{A/B}}, \mathbf{S}^{\mathrm{A/B}}\right) - \overline{\mathbf{S}}^s \times \mathfrak{g}_{\mathrm{Fe}}\mu_{\mathrm{B}}\mathbf{B}^s_{\mathrm{Er}}\left(\delta\hat{\mathfrak{s}}^{\mathrm{A/B}}, \delta\mathbf{S}^{\mathrm{A/B}}\right) \tag{21}$$

where $\delta\hat{\mathfrak{s}}^s$ and $\delta\mathbf{S}^s$ are the difference between the spin operators and their mean-field values.

These equations are solved to obtain the resonance frequencies. As coupled homogeneous linear differential equations with constant coefficients, they are solved by $\delta\hat{\mathfrak{s}}^s = \hat{\mathfrak{s}}^s(0)e^{i\omega^s_{\mathrm{Er}}t}$ and $\delta\mathbf{S}^s = \delta\mathbf{S}^s(0)e^{i\omega^s_{\mathrm{Fe}}t}$, where the frequencies ω and corresponding normal modes are found by solving a set of linear equations, $i\omega\mathfrak{s} = M\mathfrak{s}$, where $\mathfrak{s} = \left(\hat{\mathfrak{s}}^{\mathrm{A}}, \hat{\mathfrak{s}}^{\mathrm{B}}, \mathbf{S}^{\mathrm{A}}, \mathbf{S}^{\mathrm{B}}\right)$ and M is an anti-Hermitian matrix. The resonance frequencies are $-i$ times the eigenvalues of M.

Model fitting

The parameters in Eq. 5, namely, J_{Er}, $\mathfrak{g}^x_{\mathrm{Er}}$, A^x_{Er}, and A^z_{Er}, as well as A^z_{Fe} and $\mathfrak{g}^x_{\mathrm{Fe}}$ in Eq. 4, are used as fitting parameters to fit T_{c} and the spectroscopic data at $T = 2$K (Fig. 3B and fig. S10, A and B). The same set of parameters reasonably reproduces the spectroscopic data at 10 K (Fig. 3B and fig. S10C). The rest of the parameters in Eqs. 4 and 6 are the same as those used in (*21*).

We fit the calculated resonance frequencies to experimental data by minimizing a cost function with the six free parameters. The cost function reads

$$C = \sum_i \frac{w_i}{N_i}\sum_{j\in i\text{th mode}}\frac{\left(f_{ij} - \tilde{f}_{ij}\right)^2}{\tilde{f}^2_{ij}} \tag{22}$$

where i indicates the spectral modes that are fitted to; N_i is the number of experiment data points in the ith mode; j refers to the experiment data points in the ith mode; f_{ij} and $\tilde{f}_{ij}$ are the calculated and measured resonance frequencies of the ith mode at jth data point, respectively; and w_i is the weight assigned to the ith mode. The fitting is performed over five different modes: four spectral modes [the quasi-ferromagnetic (qFM) magnon mode and qAFM modes of Fe^{3+} and two Er^{3+} modes] as a function of $\mu_0 H$ at 2 K as shown in fig. S10B, and one spectral mode (qAFM mode of Fe^{3+}) as a function of T to obtain T_{c} at 0 T as shown in fig. S10A. The weights for the two Fe^{3+} (Er^{3+}) modes versus $\mu_0 H$ are 0.3 (0.1), while it is 0.2 for the qAFM mode of Fe^{3+} versus T. The fit is not very sensitive to the choice of the weights. Figure S10C shows good agreement between experimental data and calculations at 10 K using the fitted parameter values, providing confidence to our fitting protocol.

The extended Dicke model

Using spin-wave theory, the Fe^{3+} spins $S^{\mathrm{A/B}}_i$ are rewritten in terms of a set of magnonic creation and annihilation operators (a_{qFM}, a_{qAFM}, $a^{\dagger}_{\mathrm{qFM}}$, and $a^{\dagger}_{\mathrm{qAFM}}$) (*21*, *34*), where the "qFM" ("qAFM") corresponds to the $k = 0$ ($k = \pi$) quasi-momentum modes.

The magnon representation of Fe^{3+} spins is justified owing to the strong exchange interaction $J_{\mathrm{Fe}} = 4.96$ meV, making it highly dispersive, while the Er^{3+} exchange interaction, $J_{\mathrm{Er}} = 0.0132$ meV, is more than two orders of magnitude smaller. Hence, the Er^{3+} spins are well described by the collective spin approximation, and they couple only to the qAFM and qFM modes of Fe^{3+}.

The derivation of the extended Dicke model from the spin Hamiltonian follows "Derivation of extended Dicke Hamiltonian" of

(*21*). We briefly outline this here. The spin Hamiltonian is split in three parts, namely, $\widehat{\mathcal{H}}_{\mathrm{Fe}}$, $\widehat{\mathcal{H}}_{\mathrm{Er}}$, and $\widehat{\mathcal{H}}_{\mathrm{Fe-Er}}$.

First, we rewrite the Fe^{3+} subsystem in terms of magnon annihilation and creation operators. The magnons are collective spin fluctuations above mean-field configuration for the bare Fe^{3+} subsystem. The ground state is the same as previous studies (*21*, *24*, *34*)

$$\overline{\mathbf{S}}_0^{\mathrm{A}} = \begin{pmatrix} S\sin\beta_0 \\ 0 \\ -S\cos\beta_0 \end{pmatrix}, \quad \overline{\mathbf{S}}_0^{\mathrm{B}} = \begin{pmatrix} S\sin\beta_0 \\ 0 \\ S\cos\beta_0 \end{pmatrix} \tag{23}$$

where β_0 is the mean-field canting angle of the Fe^{3+} spins from the c axis (*21*, *34*)

$$\beta_0 = -\frac{1}{2}\arctan\left[\frac{z_{\mathrm{Fe}}D^y_{\mathrm{Fe}}}{z_{\mathrm{Fe}}J_{\mathrm{Fe}} - A^x_{\mathrm{Fe}} + A^z_{\mathrm{Fe}}}\right] \tag{24}$$

We neglect the non-diagonal Fe^{3+}-anisotropy term, A^{xz}_{Fe}.

Spin-wave theory yields (*21*, *34*)

$$\widehat{\mathcal{H}}_{\mathrm{Fe}} \approx \sum_{k=0,\pi} \hbar\omega_k a_k^\dagger a_k + \mathrm{const} \tag{25}$$

with $\omega_k = \mathfrak{g}_{\mathrm{Fe}}\mu_{\mathrm{B}}/\hbar\sqrt{(b\cos k - a)(d\cos k + c)}$ and

$$a = \left[S/\left(\mathfrak{g}^x_{\mathrm{Fe}}\mu_{\mathrm{B}}\right)\right]\left[-A^z_{\mathrm{Fe}} - A^x_{\mathrm{Fe}} - \left(z_{\mathrm{Fe}}J_{\mathrm{Fe}} + A^z_{\mathrm{Fe}} - A^x_{\mathrm{Fe}}\right)\cos\left(2\beta_0\right) + z_{\mathrm{Fe}}D^y_{\mathrm{Fe}}\sin\left(2\beta_0\right)\right] \tag{26}$$

$$b = \left[S/\left(\mathfrak{g}^x_{\mathrm{Fe}}\mu_{\mathrm{B}}\right)\right]z_{\mathrm{Fe}}J_{\mathrm{Fe}} \tag{27}$$

$$c = \left[S/\left(\mathfrak{g}^x_{\mathrm{Fe}}\mu_{\mathrm{B}}\right)\right]\left[\left(z_{\mathrm{Fe}}J_{\mathrm{Fe}} + 2A^z_{\mathrm{Fe}} - 2A^x_{\mathrm{Fe}}\right)\cos\left(2\beta_0\right) + z_{\mathrm{Fe}}D^y_{\mathrm{Fe}}\sin\left(2\beta_0\right)\right] \tag{28}$$

$$d = \left[S/\left(\mathfrak{g}^x_{\mathrm{Fe}}\mu_{\mathrm{B}}\right)\right]\left[-z_{\mathrm{Fe}}J_{\mathrm{Fe}}\cos\left(2\beta_0\right) - z_{\mathrm{Fe}}D^y_{\mathrm{Fe}}\sin\left(2\beta_0\right)\right] \tag{29}$$

The derivation is as is from (*21*). First, we compute the Heisenberg equations of motion of $\mathbf{S}$ for $\mathcal{H}_{\mathrm{Fe}}$. Then, we linearize them by expressing $\mathbf{S}_i^{\mathrm{A/B}} = \overline{\mathbf{S}}_0^{\mathrm{A/B}} + \delta\mathbf{S}_i^{\mathrm{A/B}}$. The effective Hamiltonian of the linearized equations of motion is decoupled harmonic oscillators. These harmonic oscillators are the magnons. The spin fluctuations in terms of ladder operators of the harmonic oscillators are

$$\delta\mathbf{S}_i^{\mathrm{A}} \approx \sqrt{\frac{S}{2N_0}}\begin{bmatrix} -\left(T_0 - T_\pi\right)\cos\beta_0 \\ \left(Y_0 - Y_\pi\right) \\ -\left(T_0 - T_\pi\right)\sin\beta_0 \end{bmatrix} \tag{30}$$

$$\delta\mathbf{S}_i^{\mathrm{B}} \approx \sqrt{\frac{S}{2N_0}}\begin{bmatrix} \left(T_0 + T_\pi\right)\cos\beta_0 \\ \left(Y_0 + Y_\pi\right) \\ -\left(T_0 + T_\pi\right)\sin\beta_0 \end{bmatrix} \tag{31}$$

where

$$T_k = \left(\frac{b\cos k - a}{d\cos k - a}\right)^{1/4}\frac{a^\dagger_{-k} + a_k}{\sqrt{2}} \tag{32}$$

$$Y_k = \left(\frac{d\cos k + c}{b\cos k - a}\right)^{1/4}\frac{i\left(a^\dagger_{-k} - a_k\right)}{\sqrt{2}} \tag{33}$$

We only keep $k = 0$ and π contributions, the qFM and qAFM modes of Fe^{3+} respectively, as there is negligible coupling to the other modes. Henceforth, these modes are labeled as a_{qFM} and a_{qAFM}.

Next, we apply the collective spin approximation on the Er^{3+} spins

$$\mathfrak{s}_i^s = \frac{1}{N_0}\sum_{j=1}^{N_0}\mathfrak{s}_j^s \tag{34}$$

$$\equiv \frac{1}{N_0}\Sigma_j^s \tag{35}$$

finding

$$\widehat{\mathcal{H}}_{\mathrm{Er}} \approx \mu_0\mu_{\mathrm{B}}\mathfrak{g}^x_{\mathrm{Er}}H^{\mathrm{DC}}_x\Sigma^+_x + z_{\mathrm{Er}}J_{\mathrm{Er}}\sum_{i=1}^{N_0}\mathfrak{s}_i^{\mathrm{A}}\cdot\sum_{i'=1}^{N_0}\frac{\mathfrak{s}^{\mathrm{B}}_{i'}}{N_0} - \sum_i\sum_{\xi=x,z}A^\xi_{\mathrm{Er}}\sum_{s=\mathrm{A,B}}\left(\frac{1}{N_0}\sum_j\mathfrak{s}^s_{j,\xi}\right)^2 \tag{36}$$

$$= \mu_0\mu_{\mathrm{B}}\mathfrak{g}^x_{\mathrm{Er}}H^{\mathrm{DC}}_x\Sigma^+_x + \frac{z_{\mathrm{Er}}J_{\mathrm{Er}}}{N_0}\Sigma^{\mathrm{A}}\cdot\Sigma^{\mathrm{B}} - \sum_{s=\mathrm{A,B}}\sum_{\xi=x,z}\frac{A^\xi_{\mathrm{Er}}}{N_0}\left(\Sigma^s_\xi\right)^2 \tag{37}$$

where $\Sigma^\pm_\xi = \Sigma^{\mathrm{A}}_\xi \pm \Sigma^{\mathrm{B}}_\xi$.

Last, we rewrite $\widehat{\mathcal{H}}_{\mathrm{Fe-Er}}$ in terms of the spin-fluctuation operators of the Fe^{3+} spins and the collective spin operators of Er^{3+} spins to give

$$\begin{aligned}\widehat{\mathcal{H}}_{\mathrm{Fe-Er}} = {} & 4S\left(J\sin\beta_0 + D_y\cos\beta_0\right)\Sigma^+_x + \left(-4SD_x\cos\beta_0\right)\Sigma^-_y \\ & + \sqrt{\frac{S}{N_0}}\Big[\left(J\cos\beta_0 - D_y\sin\beta_0\right)T_\pi\Sigma^+_x + JY_0\Sigma^+_y \\ & + \left(D_x\sin\beta_0\right)T_\pi\Sigma^-_y + D_xY_\pi\Sigma^-_z - \left(J\sin\beta_0 + D_y\cos\beta_0\right)T_0\Sigma^+_z\Big]\end{aligned} \tag{38}$$

We have different prefactors of the parameters compared to (*21*) because they have extra factors of 1/2 as the Er^{3+} spins are modeled as $1/2\sigma^s$, whereas we absorb this in our spin variables $\mathfrak{s}^s$.

The complete spin-Dicke Hamiltonian, expressed in terms of the magnonic operators and collective Er^{3+} spin operators, is

$$\begin{aligned}\widehat{\mathcal{H}}_{\mathrm{Dicke}} \approx {} & \sum_{m=\mathrm{qFM,qAFM}}\hbar\omega_m a^\dagger_m a_m + E_x\Sigma^+_x + E_y\Sigma^-_y + \mu_0\mu_{\mathrm{B}}\mathfrak{g}^x_{\mathrm{Er}}H^{\mathrm{DC}}_x\Sigma^+_x \\ & + \frac{z_{\mathrm{Er}}J_{\mathrm{Er}}}{N_0}\Sigma^{\mathrm{A}}\cdot\Sigma^{\mathrm{B}} - \sum_{\xi=x,z}\sum_{s=\mathrm{A,B}}\frac{A^\xi_{\mathrm{Er}}}{N_0}\left(\Sigma^s_\xi\right)^2 + \frac{\hbar g_x}{\sqrt{N_0}}\left(a^\dagger_{\mathrm{qAFM}} + a_{\mathrm{qAFM}}\right)\Sigma^+_x \\ & + \frac{i\hbar g_y}{\sqrt{N_0}}\left(a^\dagger_{\mathrm{qFM}} - a_{\mathrm{qFM}}\right)\Sigma^+_y + \frac{\hbar g_{y'}}{\sqrt{N_0}}\left(a^\dagger_{\mathrm{qAFM}} + a_{\mathrm{qAFM}}\right)\Sigma^-_y \\ & + \frac{i\hbar g_z}{\sqrt{N_0}}\left(a^\dagger_{\mathrm{qAFM}} - a_{\mathrm{qAFM}}\right)\Sigma^-_z + \frac{\hbar g_{z'}}{\sqrt{N_0}}\left(a^\dagger_{\mathrm{qFM}} + a_{\mathrm{qFM}}\right)\Sigma^+_z\end{aligned} \tag{39}$$

$E_x = 4S\left(J\sin\beta_0 + D_y\cos\beta_0\right) = h\times 0.0147341$ THz, $E_y = -4SD_x\cos\beta_0 = h\times(-0.16999041)$ THz, and the five coupling strengths are

$$\hbar g_x = \sqrt{xS}\left(J\cos\beta_0 - D_y\sin\beta_0\right)\left(\frac{b+a}{d-c}\right)^{1/4} = h\sqrt{x}\times 0.037\ \text{THz} \tag{40}$$

$$\hbar g_y = \sqrt{xS}J\left(\frac{d+c}{b-a}\right)^{1/4} = h\sqrt{x}\times 0.031\ \text{THz} \tag{41}$$

$$\hbar g_{y'} = \sqrt{xS}D_x\sin\beta_0\left(\frac{b+a}{d-c}\right)^{1/4} = h\sqrt{x}\times 2.28\times 10^{-5}\ \text{THz} \tag{42}$$

$$\hbar g_z = \sqrt{xS}D_x\left(\frac{d-c}{b+a}\right)^{1/4} = h\sqrt{x}\times 0.079\ \text{THz} \tag{43}$$

$$\hbar g_{z'} = \sqrt{xS}\left(-J\sin\beta_0 - D_y\cos\beta_0\right)\left(\frac{b-a}{d+c}\right)^{1/4} = h\sqrt{x}\times -0.026109848\ \text{THz} \tag{44}$$

$x = \tanh\left[\frac{|E_x+\mu_0\mu_B\mathfrak{g}^x_{\text{Er}}H^{\text{DC}}_x|}{2k_BT}\right]$ is the spin-dilution factor that incorporates the effect of temperature (*21*). We find that $\left\langle\Sigma^{\pm}_y\right\rangle \approx 0$. The role of the bare bosonic frequency, ω_0, is played by $\omega_{\text{qAFM}} = 2\pi\times 0.956$ THz and that of the bare atomic frequency, ω_a, is played by $\mu_B\mu_0\mathfrak{g}^x_{\text{Er}}H^{\text{DC}}_x/\hbar$ and, hence, controlled by the magnetic field. The largest coupling constant, g_z, dictates the important Dicke physics of the SRPT. The other coupling constants merely fine-tune the exact location of the SRPT. We note that the magnon mode responsible for the SRPT is not the qFM mode but the qAFM mode. The qFM mode couples with the Σ^+_z component with a coupling strength of $g_{z'}$ that is small compared with other coupling strengths. Additionally, because our experiments have been performed in $\vec{H}_{\text{DC}} \parallel a$, the $\left\langle\Sigma^+_z\right\rangle$ is negligible in the ground state in both Γ_{12} and Γ_2 phases. Therefore, the contribution of qFM mode is negligible or at most would contribute to the renormalization of the SR-phase boundary.

Supplementary Materials

This PDF file includes:

Supplementary Text
Figs. S1 to S11
Table S1
References

REFERENCES AND NOTES

1. R. H. Dicke, Coherence in spontaneous radiation processes. *Phys. Rev.* **93**, 99–110 (1954).
2. B. M. Garraway, The Dicke model in quantum optics: Dicke model revisited. *Philos. Transact. A Math. Phys. Eng. Sci.* **369**, 1137–1155 (2011).
3. P. Forn-Díaz, L. Lamata, E. Rico, J. Kono, E. Solano, Ultrastrong coupling regimes of light-matter interaction. *Rev. Mod. Phys.* **91**, 025005 (2019).
4. A. Frisk Kockum, A. Miranowicz, S. De Liberato, S. Savasta, F. Nori, Ultrastrong coupling between light and matter. *Nat. Rev. Phys.* **1**, 19–40 (2019).
5. K. Cong, Q. Zhang, Y. Wang, G. T. Noe, A. Belyanin, J. Kono, Dicke superradiance in solids. *J. Opt. Soc. Am. B* **33**, C80–C101 (2016).
6. N. Marquez Peraca, A. Baydin, W. Gao, M. Bamba, J. Kono, "Ultrastrong light-matter coupling in semiconductors" in *Semiconductor Quantum Science and Technology*, M. Kira, S. T. Cundiff, Eds. (Elsevier, 2020), vol. 105, pp. 89–151.
7. F. Schlawin, D. M. Kennes, M. A. Sentef, Cavity quantum materials. *Appl. Phys. Rev.* **9**, 011312 (2022).
8. V. Buzžek, M. Orszag, M. Rosško, Instability and entanglement of the ground state of the Dicke model. *Phys. Rev. Lett.* **94**, 163601 (2005).
9. K. Hepp, E. H. Lieb, On the superradiant phase transition for molecules in a quantized radiation field: The Dicke maser model. *Ann. Phys.* **76**, 360–404 (1973).
10. Y. K. Wang, F. T. Hioe, Phase transition in the Dicke model of superradiance. *Phys. Rev. A* **7**, 831–836 (1973).
11. D. S. Shapiro, W. V. Pogosov, Y. E. Lozovik, Universal fluctuations and squeezing in a generalized Dicke model near the superradiant phase transition. *Phys. Rev. A* **102**, 023703 (2020).
12. P. Nataf, C. Ciuti, No-go theorem for superradiant quantum phase transitions in cavity QED and counter-example in Circuit QED. *Nat. Commun.* **1**, 72 (2010).
13. M. Bamba, K. Inomata, Y. Nakamura, Superradiant phase transition in a superconducting circuit in thermal equilibrium. *Phys. Rev. Lett.* **117**, 173601 (2016).
14. P. Kirton, M. M. Roses, J. Keeling, E. G. Dalla Torre, Introduction to the Dicke model: From equilibrium to nonequilibrium, and *vice versa*. *Adv. Quantum Technol.* **2**, 1800043 (2019).
15. L. Garziano, A. Settineri, O. Di Stefano, S. Savasta, F. Nori, Gauge invariance of the Dicke and Hopfield models. *Phys. Rev. A* **102**, 023718 (2020).
16. D. Lamberto, O. D. Stefano, S. Hughes, F. Nori, S. Savasta, Quantum phase transitions in many-dipole light-matter systems. arXiv:2405.10711 (2024).
17. D. Lamberto, G. Orlando, S. Savasta, Superradiant quantum phase transition in open systems: System-bath interaction at the critical point. arXiv:2411.16514 (2024).
18. K. Rzażewski, K. Wódkiewicz, W. Żakowicz, Phase transitions, two-level atoms, and the A^2 term. *Phys. Rev. Lett.* **35**, 432–434 (1975).
19. G. M. Andolina, F. M. D. Pellegrino, V. Giovannetti, A. H. MacDonald, M. Polini, Cavity quantum electrodynamics of strongly correlated electron systems: A no-go theorem for photon condensation. *Phys. Rev. B* **100**, 121109 (2019).
20. P. Nataf, T. Champel, G. Blatter, D. M. Basko, Rashba cavity QED: A route towards the superradiant quantum phase transition. *Phys. Rev. Lett.* **123**, 207402 (2019).
21. M. Bamba, X. Li, N. Marquez Peraca, J. Kono, Magnonic superradiant phase transition. *Commun. Phys.* **5**, 3 (2022).
22. X. Li, M. Bamba, Q. Zhang, S. Fallahi, G. C. Gardner, W. Gao, M. Lou, K. Yoshioka, M. J. Manfra, J. Kono, Vacuum Bloch–Siegert shift in Landau polaritons with ultra-high cooperativity. *Nat. Photonics* **12**, 324–329 (2018).
23. S. Hughes, C. Gustin, F. Nori, Reconciling quantum and classical spectral theories of ultrastrong coupling: Role of cavity bath coupling and gauge corrections. *Opt. Quantum* **2**, 133–139 (2024).
24. X. Li, M. Bamba, N. Yuan, Q. Zhang, Y. Zhao, M. Xiang, K. Xu, Z. Jin, W. Ren, G. Ma, S. Cao, D. Turchinovich, J. Kono, Observation of Dicke cooperativity in magnetic interactions. *Science* **361**, 794–797 (2018).
25. N. Marquez Peraca, X. Li, J. M. Moya, K. Hayashida, D. Kim, X. Ma, K. J. Neubauer, D. F. Padilla, C. L. Huang, P. Dai, A. H. Nevidomskyy, H. Pu, E. Morosan, S. Cao, M. Bamba, J. Kono, Quantum simulation of an extended Dicke model with a magnetic solid. *Commun. Mater.* **5**, 42 (2024).
26. T. Makihara, K. Hayashida, G. T. Noe II, X. Li, N. Marquez Peraca, X. Ma, Z. Jin, W. Ren, G. Ma, I. Katayama, J. Takeda, H. Nojiri, D. Turchinovich, S. Cao, M. Bamba, J. Kono, Ultrastrong magnon–magnon coupling dominated by antiresonant interactions. *Nat. Commun.* **12**, 3115 (2021).
27. K. Hayashida, T. Makihara, N. Marquez Peraca, D. Fallas Padilla, H. Pu, J. Kono, M. Bamba, Perfect intrinsic squeezing at the superradiant phase transition critical point. *Sci. Rep.* **13**, 2526 (2023).
28. J. M. Lee, H.-W. Lee, M.-J. Hwang, Cavity magnonics with easy-axis ferromagnets: Critically enhanced magnon squeezing and light-matter interaction. *Phys. Rev. B* **108**, L241404 (2023).
29. H. Yuan, Y. Cao, A. Kamra, R. A. Duine, P. Yan, Quantum magnonics: When magnon spintronics meets quantum information science. *Phys. Rep.* **965**, 1–74 (2022).
30. L. Liensberger, A. Kamra, H. Maier-Flaig, S. Geprägs, A. Erb, S. T. B. Goennenwein, R. Gross, W. Belzig, H. Huebl, M. Weiler, Exchange-enhanced ultrastrong magnon-magnon coupling in a compensated ferrimagnet. *Phys. Rev. Lett.* **123**, 117204 (2019).
31. A. Kamra, W. Belzig, A. Brataas, Magnon-squeezing as a niche of quantum magnonics. *Appl. Phys. Lett.* **117**, 090501 (2020).
32. C. Emary, T. Brandes, Quantum chaos triggered by precursors of a quantum phase transition: The Dicke model. *Phys. Rev. Lett.* **90**, 044101 (2003).
33. X. Li, D. Kim, Y. Liu, J. Kono, Terahertz spin dynamics in rare-earth orthoferrites. *Photon. Insights* **1**, R05 (2022).
34. G. Herrmann, Resonance and high frequency susceptibility in canted antiferromagnetic substances. *J. Phys. Chem. Solid* **24**, 597–606 (1963).
35. V. Klochan, N. Kovtun, V. Khmara, Low-temperature spin configuration of iron ions in erbium orthoferrite. *Sov. Phys. JETP* **41**, 357 (1975).
36. M. P. Zic, W. T. Fuhrman, K. Wang, S. Ran, J. Paglione, N. P. Butch, Coupled spin waves and crystalline electric field levels in candidate multiferroic $ErFeO_3$. *J. Appl. Phys.* **130**, 014102 (2021).
37. R. L. White, Review of recent work on the magnetic and spectroscopic properties of the rare-earth orthoferrites. *J. Appl. Phys.* **40**, 1061–1069 (1969).
38. A. M. Kadomtseva, I. B. Krynetskiĭ, V. M. Matveev, Nature of the spontaneous and field-induced low-temperature orientational transitions in erbium orthoferrite. *J. Exp. Theor. Phys.* **52**, 732–737 (1980).

39. I. M. Vitebskiĭ, N. K. Danshin, A. I. Izotov, M. A. Sdvizhkov, L. T. Tsymbal, Anomalous critical dynamics of a low-temperature transition in erbium orthoferrite. *J. Exp. Theor. Phys.* **71**, 187–190 (1990).
40. A. Baydin, T. Makihara, N. M. Peraca, J. Kono, Time-domain terahertz spectroscopy in high magnetic fields. *Front. Optoelectron.* **14**, 110–129 (2021).
41. G. F. Herrmann, Magnetic resonances and susceptibility in orthoferrites. *Phys. Rev.* **133**, A1334 (1964).
42. K. Yamaguchi, T. Kurihara, Y. Minami, M. Nakajima, T. Suemoto, Terahertz time-domain observation of spin reorientation in orthoferrite $ErFeO_3$ through magnetic free induction decay. *Phys. Rev. Lett.* **110**, 137204 (2013).
43. V. G. Baryakhtar, I. M. Vitebeskiĭ, D. A. Yablonskiĭ, Theory of metamagnetic phase transitions. *Sov. Phys. Solid State* **19**, 1249–1254 (1977).
44. N. K. Danshin, V. N. Derkachenko, N. M. Kovtun, M. A. Sdvizhkov, Metamagnetic phase transition in $ErFeO_3$. *Sov. Phys. Solid State* **28**, 1461–1464 (1986).
45. D. L. Wood, L. M. Holmes, J. P. Remeika, Exchange fields and optical Zeeman effect in $ErFeO_3$. *Phys. Rev.* **185**, 689–695 (1969).
46. A. K. Zvezdin, A. A. Muchin, A. I. Popov, Magnetic-structure instability resulting from the intersection of energy levels. *JETP Lett.* **23**, 240 (1976).
47. D. Porras, P. A. Ivanov, F. Schmidt-Kaler, Quantum simulation of the cooperative Jahn-Teller transition in 1D ion crystals. *Phys. Rev. Lett.* **108**, 235701 (2012).
48. M. Hagiwara, K. Katsumata, H. Yamaguchi, M. Tokunaga, I. Yamada, M. Gross, P. Goy, A complete frequency-field chart for the antiferromagnetic resonance in MnF_2. *Int. J. Infrared and Mill.* **20**, 617–622 (1999).
49. X. X. Zhang, Z. C. Xia, Y. J. Ke, X. Q. Zhang, Z. H. Cheng, Z. W. Ouyang, J. F. Wang, S. Huang, F. Yang, Y. J. Song, G. L. Xiao, H. Deng, D. Q. Jiang, Magnetic behavior and complete high-field magnetic phase diagram of the orthoferrite $ErFeO_3$. *Phys. Rev. B* **100**, 054418 (2019).
50. K. P. Belov, A. K. Zvezdin, A. M. Kadomtseva, R. Z. Levitin, Spin-reorientation transitions in rare-earth magnets. *Sov. Phys. Usp.* **19**, 574–596 (1976).
51. A. M. Balbashov, G. V. Kozlov, A. A. Mukhin, A. S. Prokhorov, "Submillimeter spectroscopy of antiferromagnetic dielectrics: Rare-earth orthoferrites" in *High Frequency Processes in Magnetic Materials* (World Scientific Publishing, 1995), pp. 56–91.
52. V. D. Buchelnikov, N. K. Danshin, L. T. Tsymbal, V. G. Shavrov, Magnetoacoustics of rare-earth orthoferrites. *Phys Uspekhi* **39**, 547–572 (1996).
53. J. Zhang, "Microwave spectroscopy on two dimensional electron/hole gases," thesis, Rice University, Houston, TX (2018).
54. T. E. Kritzell, A. Baydin, F. Tay, R. Rodriguez, J. Doumani, H. Nojiri, H. O. Everitt, I. Barsukov, J. Kono, Terahertz cavity magnon polaritons. *Adv. Opt. Mater.* **12**, 2302270 (2024).
55. K. W. Vugrin, L. P. Swiler, R. M. Roberts, N. J. Stucky-Mack, S. P. Sullivan, Confidence region estimation techniques for nonlinear regression in groundwater flow: Three case studies. *Water Resour. Res.* **43**, W03423 (2007).

Acknowledgments

Funding: D.K. and J.K. acknowledge support from the U.S. Army Research Office (through award no. W911NF2110157), the Gordon and Betty Moore Foundation (through grant no. 11520), and the Robert A. Welch Foundation (through grant no. C-1509). K.R.A.H. and J.K. acknowledge support from the W. M. Keck Foundation (through award no. 995764). D.K. and J.K. acknowledge support from Global Institute for Materials Research Tohoku and International Collaborations with Institute for Materials Research, Tohoku University. K.R.A.H. acknowledges support from the National Science Foundation (PHY-1848304). M.B. acknowledges support from the Japan Society for the Promotion of Science (through grant nos. JPJSJRP20221202 and JP24K21526) and from the Research Foundation for Opto-Science and Technology. L.L., J.-M.P., D.C., R.H.J.K., and J.W. were supported by the US Department of Energy, Office of Basic Energy Science, Division of Materials Sciences and Engineering (Ames National Laboratory is operated for the US Department of Energy by Iowa State University under contract no. DE-AC02-07CH11358). S.C. acknowledges support from the National Natural Science Foundation of China (NSFC; no. 12374116). **Author contributions:** J.K. conceived and supervised the project. D.K. conceived detailed experimental plans, performed THz measurements and GHz temperature measurements, analyzed all experimental data, and prepared the manuscript under the supervision and guidance of J.K. S.D. and H.-T.W. derived the spin Hamiltonian and the extended Dicke model, introduced the anisotropy term, and performed fitting under the supervision and guidance of M.B. and K.R.A.H. M.B. developed the theoretical model. X.M. and W.Y. grew, cut, and characterized the crystals used in the experiments under the guidance of S.C. J.D. polished the samples under the guidance of J.K. J.-M.P. performed THz measurements and GHz temperature measurements. L.L., J.-M.P., D.C., and R.H.J.K. built the THz setup under the guidance of J.W. H.N., S.K., and D.K. performed GHz transmission measurements. All authors discussed the results and commented on the manuscript. **Competing interests:** The authors declare that they have no competing interests. **Data and materials availability:** All data needed to evaluate the conclusions in the paper are present in the paper and/or the Supplementary Materials.

Submitted 14 September 2024
Accepted 28 February 2025
Published 4 April 2025
10.1126/sciadv.adt1691

Science Advances
AAAS

Supplementary Materials for

Observation of the magnonic Dicke superradiant phase transition

Dasom Kim *et al.*

Corresponding author: Shixun Cao, sxcao@shu.edu.cn; Junichiro Kono, kono@rice.edu

Sci. Adv. **11**, eadt1691 (2025)
DOI: 10.1126/sciadv.adt1691

This PDF file includes:

Supplementary Text

S1. SRPT at finite detuning

An anti-crossing of two polaritons occurs at the zero-detuning point ($\omega_0 = \omega_a$). When the normalized coupling strength ($\eta \equiv g/\omega_0$) reaches the critical value of 0.5, the system undergoes the SRPT, and ω_- becomes zero. As shown in fig. S1A, for $\eta = 0.5$ the SRPT occurs when $\omega_0 = \omega_a$. For $\eta = 0.1$ (fig. S1B), a situation more comparable to $ErFeO_3$, we find the phase boundary moves to the $\omega_a < \omega_0$, while the anti-crossing still occurs at the zero-detuning point. Thus one can achieve the SRPTs with a small η as long as $\nu \equiv \omega_a/\omega_0$ is small enough to satisfy the Eq. 2. By contrast, when $\nu > 1$, the η_c becomes higher than 0.5.

S2. THz absorption spectra at high temperatures

Figure S6A shows temperature-dependent absorption spectra of the qAFM mode of Fe^{3+}. The kink occurs at 4 K which is the SR-phase boundary at 0 T. Below this temperature, the Fe^{3+} order parameter $\langle S_y^{A/B} \rangle$ becomes finite. Figure S6B shows magnetic field dependence of the qAFM mode of Fe^{3+} at 10 K. Only a slight change was observed at low magnetic fields without any signature of the phase transition, consistent with our phase diagram. Meanwhile, two modes that emerge at high fields are Er^{3+} EPR modes. As described in main text, $ErFeO_3$ can be modeled by the two-sublattice model. This implies we should expect four modes in total: the qFM and qAFM modes for Fe^{3+} spins, and in-phase and out-of-phase EPR modes for Er^{3+} spins. Here, we are considering the relative phase of precession of two Er^{3+} spins. A detailed derivation is in Materials and Methods and follows that in Ref. (*21*). Our theory finds the lowest mode is the out-of-phase mode that is coupled to qAFM, establishing a magnon-spin system. Due to the polarization selection rule described in Fig. 2B, the qFM mode does not appear in fig. S6.

S3. Spectroscopic evidence of hybridization at zero-detuning

A direct spectroscopic signature of the hybridization of the Fe^{3+} qAFM mode and the lower Er^{3+} EPR mode would be an anticrossing behavior in the frequencies, $\omega_\pm$, of the upper- and lower-polariton branches, as a function of magnetic field, H_{DC}. Figure S2 shows calculated $\omega_\pm$ in H_{DC} up to 20 T, exhibiting an anticrossing behavior around the zero-detuning point at ~17 T. However,

experimentally, the field range of the THz time-domain magnetospectroscopy setup used was limited to 7 T in the Voigt geometry ($\vec{k}_{\mathrm{THz}} \perp \vec{H}_{\mathrm{DC}}, \vec{k}_{\mathrm{THz}} \parallel b$), which is required for realizing a $\vec{H}_{\mathrm{THz}} \parallel \vec{H}_{\mathrm{DC}} \parallel a$ configuration needed for a b-cut crystal. Nonetheless, we conducted experiments in the Faraday geometry ($\vec{k}_{\mathrm{THz}} \parallel \vec{H}_{\mathrm{DC}} \parallel c$, $\vec{H}_{\mathrm{THz}} \parallel a$) with a c-cut crystal and were able to observe an anticrossing. This was possible because the z component of the Landé g-factor of Er^{3+} spins is larger than the x component, which lowers the zero-detuning magnetic field to an accessible range. Figure S3 shows transmission decrease as a function of magnetic field and frequency at 1.4 K, in which a pronounced anticrossing is observed at around 7 T. This coupling is modeled by g_z (or D_x) in Eqs. 11, 39, and 43, which is a coupling between the qAFM and the Er^{3+} EPR mode (out-of-phase). This is the coupling that is responsible for the $\Gamma_2 \rightarrow \Gamma_{12}$ phase transition, highlighting the importance of hybridization in the phase transition. We also note that the brightest mode (the solid line) is the in-phase Er^{3+} EPR mode.

S4. Justification of the magnonic SRPT

We provide additional justification as to why the phase transition we observed, described by the extended Dicek model, is indeed equivalent to the conventional Dicke SRPT. As stated earlier, the most important term for Dicke-type interaction is the x-component of the Fe^{3+}–Er^{3+} antisymmetric exchange interaction, D_x. This becomes clear if we set all the other Fe^{3+}–Er^{3+} couplings (J and D_y) and all the Er^{3+}-spin terms (J_{Er} and $A_{\mathrm{Er}}^{x/z}$) to be zero; then the extended Dicke model of Eq. 39 becomes the simple Dicke model. We demonstrate our claim that the observed phases and SRPT are equivalent to the simple Dicke model by showing that the phase diagram of the extended Dicke model is adiabatically connected to that of the simple Dicke model.

Figure S4 shows this equivalence. We define a parameter λ that interpolates between the extended Dicke Hamiltonian ($\lambda = 1$) and the simple Dicke model ($\lambda = 0$). Specifically, we define a Hamiltonian extending Eq. 39 such that

$$H_{\mathrm{interp}}[\lambda] = H[J_{\mathrm{Fe}}, D_{\mathrm{Fe}}^{y}, A_{\mathrm{Fe}}^{x/z}, D_x, \lambda J_{\mathrm{Er}}, \lambda A_{\mathrm{Er}}^{x/z}, \lambda J, \lambda D_y]. \tag{S1}$$

We plot the Fe^{3+}-canting order parameter, $\langle S_y^{\mathrm{A/B}} \rangle$ at $H_{\mathrm{DC}} = 0$ as functions of D_x and λ in fig. S4A. In figs. S4A and B, we see that the ordered and disordered phases of the extended Dicke model ($\lambda = 1$) continuously evolve into those of the simple Dicke model ($\lambda = 0$). The top panel of fig. S4C

shows the $\lambda = 0$ cut of fig. S4A where two order parameters (Fe^{3+} and Er^{3+}) are finite above a certain critical point, and highlights the important role of D_x. The $D_x = 0$ cut reveals that while the Er^{3+} order parameter is finite above a certain critical point, the Fe^{3+} order parameter is always zero in the absence of the D_x interaction, highlighting the necessity of D_x (fig. S4C, bottom panel). Figure S4A shows a trajectory smoothly connects a conventional Dicke SR phase (green star) to the experimental SR phase (blue star). Figure S4B shows a critical magnetic field strength along the way from the green star to the blue star, which confirms the adiabatic connection of our SR phase to the conventional SR phase.

The "non-Dicke" terms do not change the qualitative features of the spectrum. To show how the additional terms in the extended Dicke model affect the phase transition, we set a finite value of $D_x = 0.045$ meV, and plot the spectrum for $\lambda = 0$ (fig. S5). With the D_x term alone, we confirm the occurence of the SRPT, and the kink and softening in the two polariton branches, respectively. Subsequently, we set each additional terms to a non-zero value one at a time, and observe how the critical magnetic field shifts. Figure S5 shows reduced the size of the SR phase with the inclusion of the D_y, A^x_{Er}, and J terms. It is the J term that governs the $\sim \mathbf{S} \cdot \mathfrak{s}$ interaction. It also shows an increased size of the SR phase with the inclusion of the J_{Er} term (atom–atom interaction) and A^z_{Er} term. We conclude that the J_{Er} and A^z_{Er} terms enhance the SR phase, whereas the J, D_y, and A^x_{Er} terms suppress it.

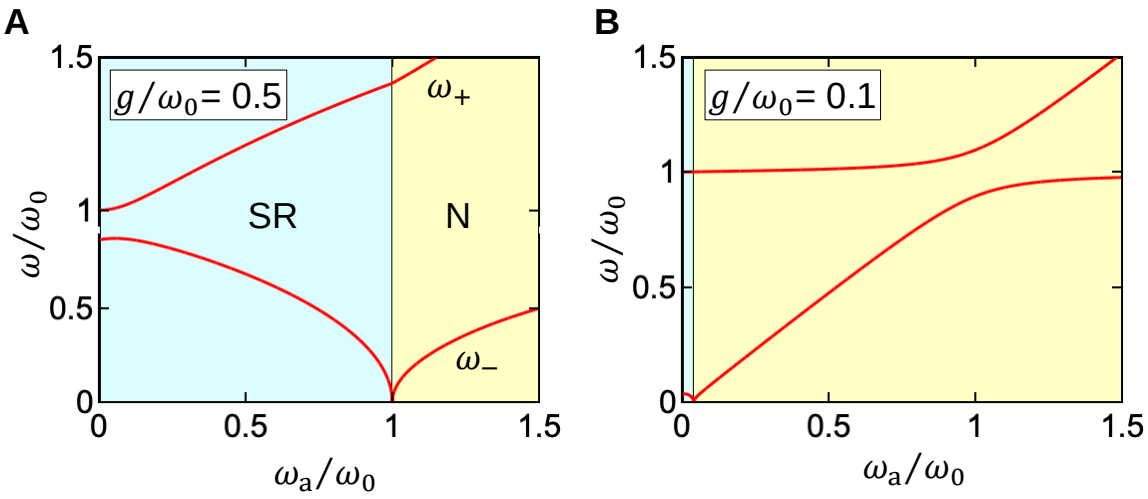

Figure S1: **Occurrence of the superradiant phase transition at finite detuning.** (**A** and **B**), Normalized frequencies of the upper-polariton (ω_+) and lower-polariton (ω_-) modes as a function of ω_a/ω_0 calculated using the Dicke model without the A^2 term with $g/\omega_0 = 0.5$ (**A**) and with $g/\omega_0 = 0.1$ (**B**).

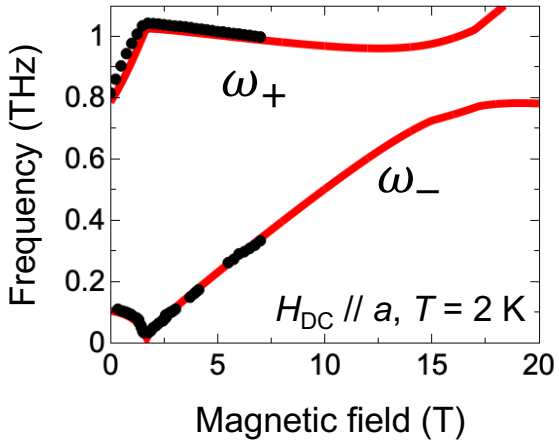

Figure S2: **Calculated resonance frequencies of the upper- and lower-polariton branches, ω_+ and ω_-, respectively, as a function of magnetic field up to 20 T applied along the a-axis.** An anticrossing behavior is seen around the zero-detuning point at ~17 T. Solid circles: experimental data.

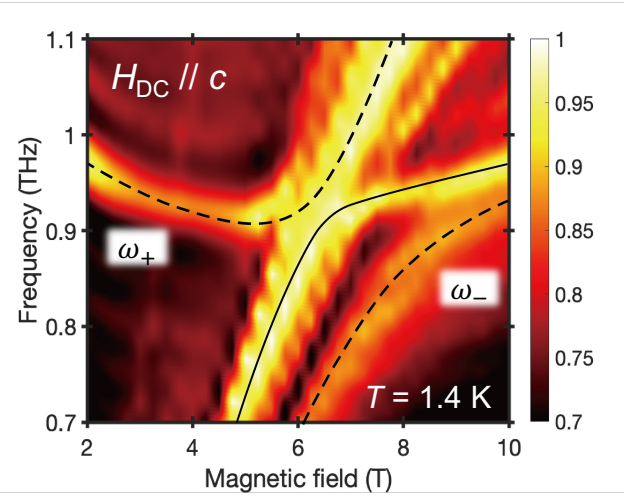

Figure S3: **Transmission decrease** $(1 - \tilde{T})$ **as a function of magnetic field applied parallel to the** c **axis at 1.4 K.** The Fe^{3+} qAFM and Er^{3+} EPR modes are hybridized, creating the upper- and lower-polariton branches ($\omega_{\pm}$); the lines are a guide to the eye.

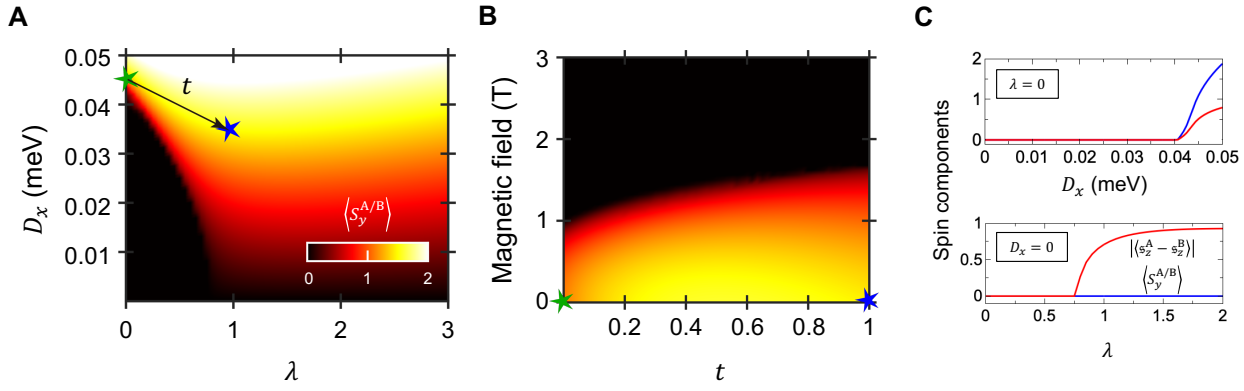

Figure S4: $T = 2$ **K zero-field phase diagram.** (**A**) The Fe^{3+} order parameters as a function of D_x and λ. (**B**) The Fe^{3+} order parameters as a function of external magnetic field and the parametric variable t, which parameterizes the λ-D_x trajectory shown in (**A**). (**C**) (Top) $\lambda = 0$ cut of (**A**), (bottom) $D_x = 0$ cut of (**A**). We can see clearly that the Fe^{3+} order parameters are independent of varying of λ.

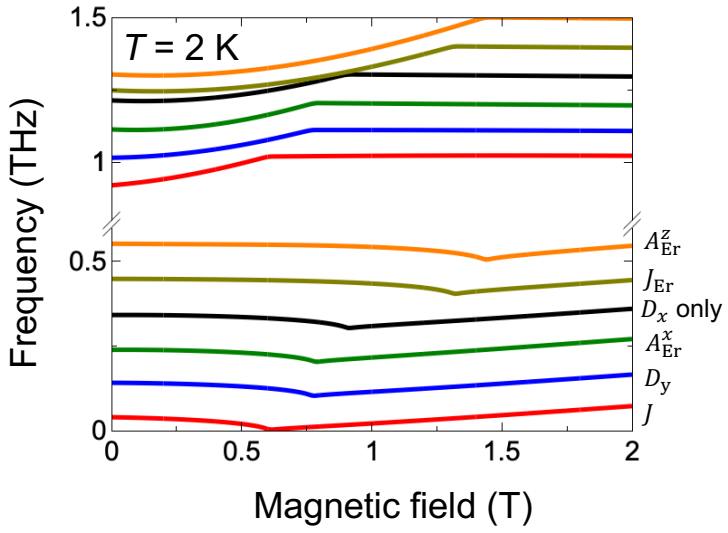

Figure S5: **Effects of the "non-Dicke" parameters on the polariton spectra calculated in $\vec{H}_{DC} \parallel a$ at 2 K.** The upper six curves are upper-polariton branches and the lower six curves are corresponding lower-polariton branches. The curves are offset by 0.1 for clarity. J_{Fe}, D^x_{Fe}, and $A^{x/z}_{Fe}$ are the same as provided in the main text. D_x only: $D_x = 0.045$ meV and $J = D_y = J_{Er} = A^x_{Er} = A^z_{Er} = 0$; J, D_y, and J_{Er}: Addition of J, D_y, and J_{Er} (twice smaller than the value shown in table S1) to the D_x only case, respectively; $A^{x/z}_{Er}$: Addition of $A^{x/z}_{Er}$ (five times smaller than the value shown in table S1) to the D_x only case. The addition of J, D_y, and A^x_{Er} weakens the SR-phase boundary. The addition of J_{Er} and A^z_{Er} strengthens the SR-phase boundary.

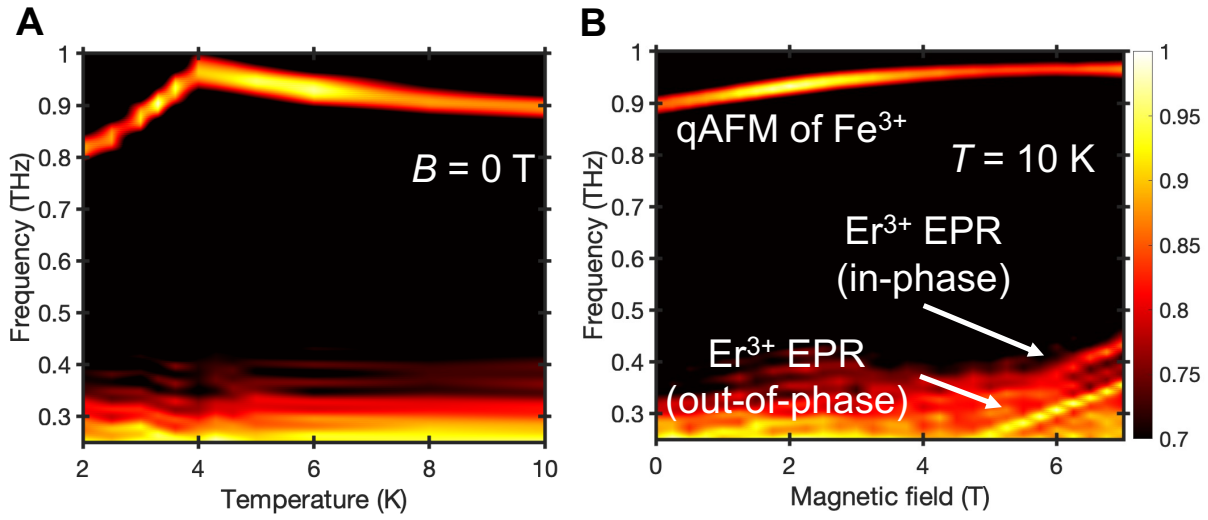

Figure S6: **Terahertz transmission decrease** $(1 - \tilde{T})$ **spectra.** (**A**) transmission decrease as a function of temperature in THz-TDS, showing a kink at the phase boundary. (**B**) transmission decrease as a function of the magnetic field in THz-TDMS. The qAFM mode of Fe^{3+} and two Er^{3+} EPR modes are observed. Fig. 3B (right panel) plots the out-of-phase mode. Our mean-field calculation in Fig. S10C shows all three modes.

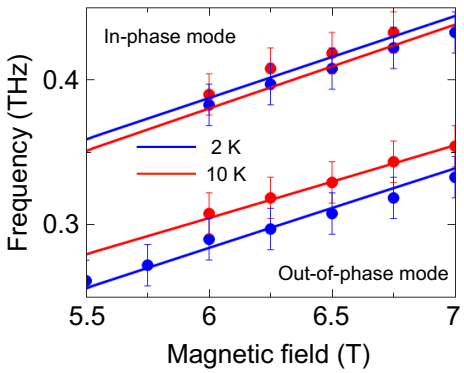

Figure S7: **In-phase and out-of-phase modes of** Er^{3+} **spins below and above the critical temperature, showing shifts only for the 2 K case.** Blue color: 2 K, red color: 10 K, lines: theory, circles: experimental data. The error bars indicate a frequency resolution determined by the time window (Δf = 1/33 ps = 0.0286 THz).

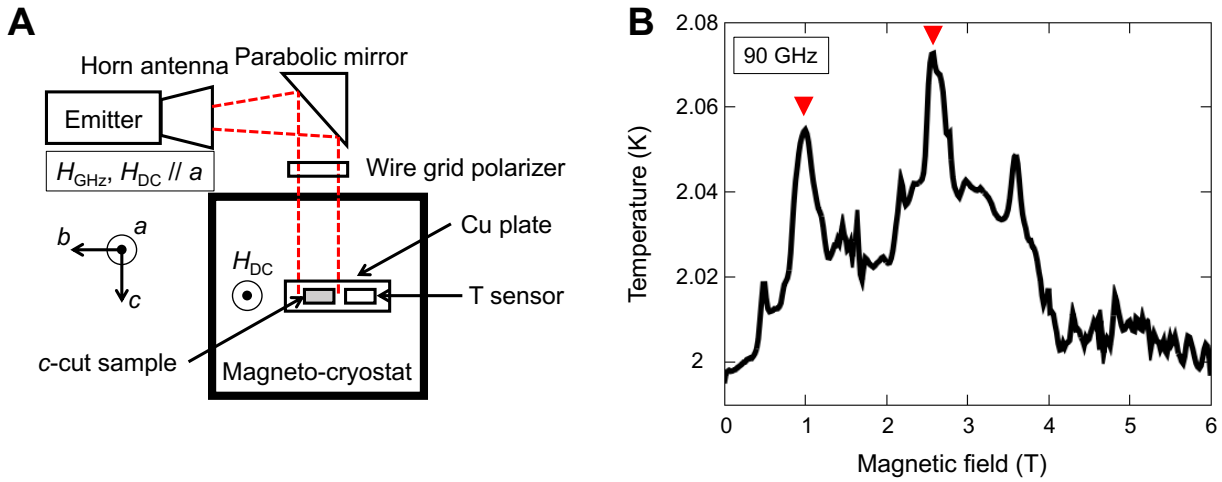

Figure S8: **Thermal detection of Er^{3+} EPR modes.** (**A**) A schematic of the setup for thermal detection. (**B**) The sample temperature as a function of the static magnetic field with 90 GHz illumination. The temperature increases when the incident photon energy coincides with the transition energy of magnetic resonances.

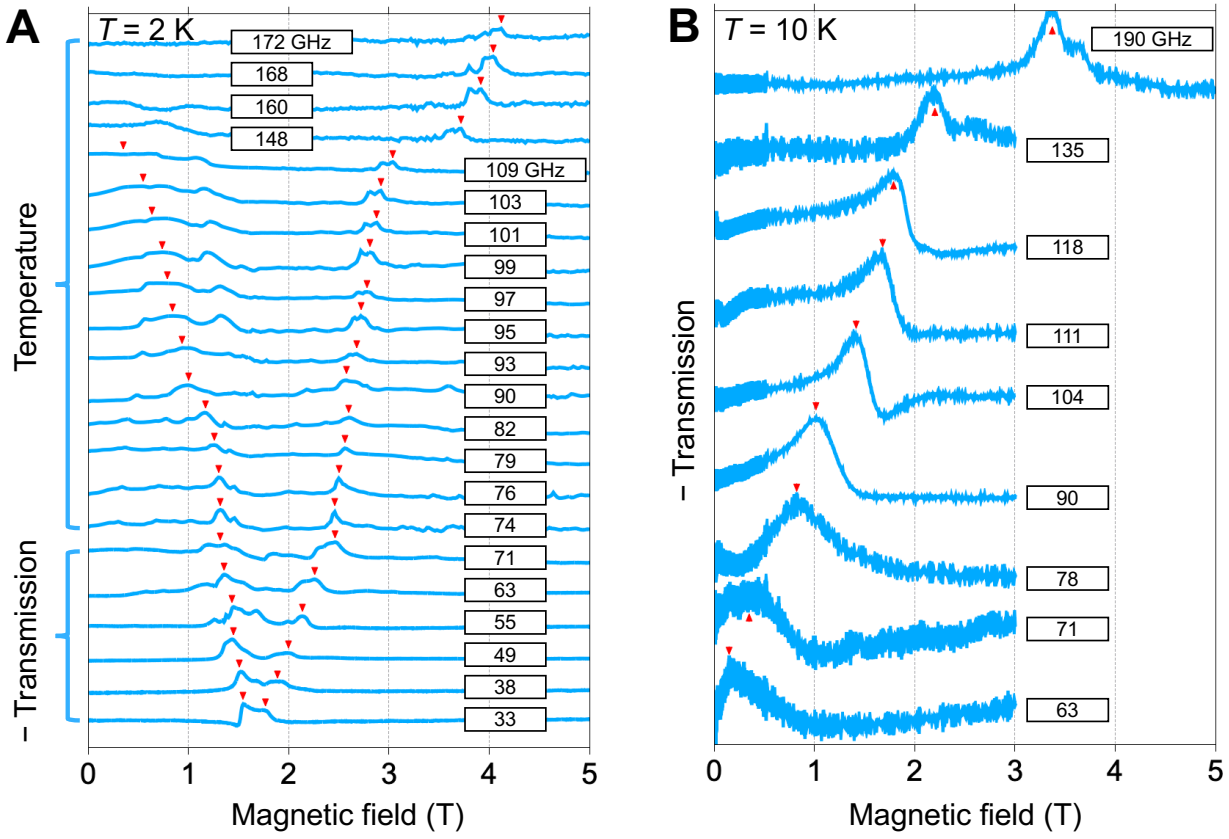

Figure S9: **Raw data of GHz measurements with 0-to-1 scale.** (**A**) From 33 to 71 GHz (74 to 172 GHz), transmission (temperature) spectra as a function of the magnetic field at 2 K. These data are used to generate the two middle and bottom panels in Fig. 2C. (**B**) From 63 to 190 GHz, transmission spectra as a function of the magnetic field at 10 K. Red triangles indicate the resonance peak positions in Fig. 3B (right panel, red circles).

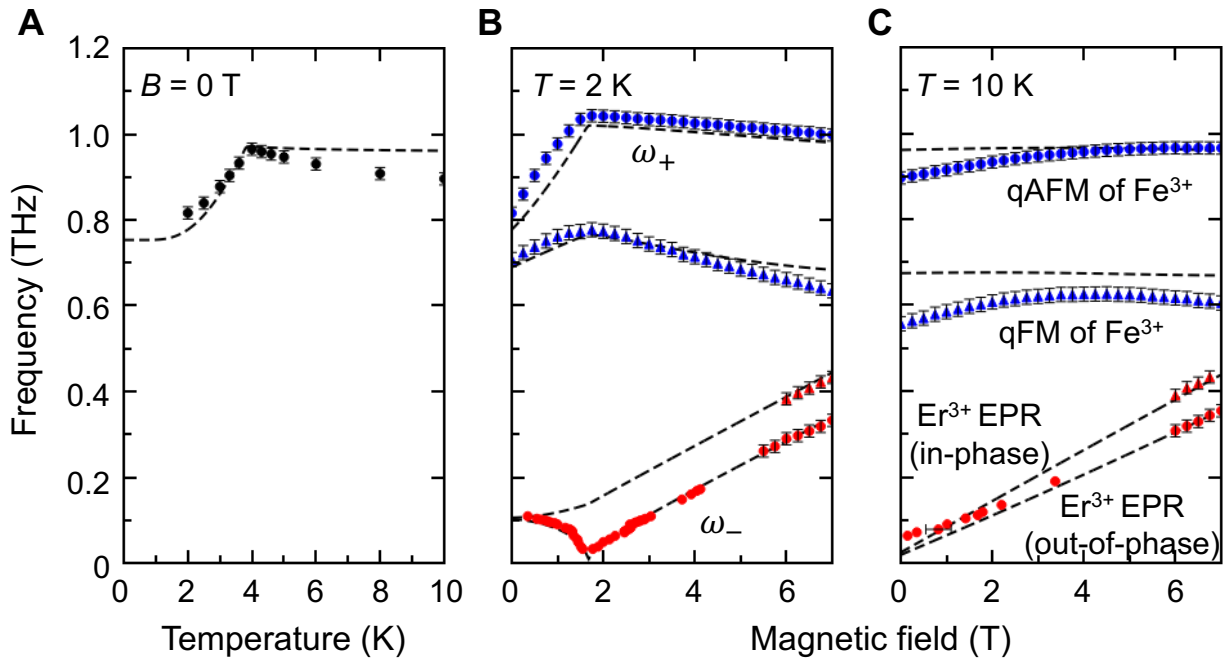

Figure S10: **Comparison between experimental data and fitting results.** (**A**) Temperature dependent absorption peaks of the qAFM mode of Fe^{3+} extracted from Fig. S6A. (**B** and **C**) Magnetic field dependent absorption peaks of all four modes at 2 K (**B**) and at 10 K (**C**). We present our fitting curves in (**A**) and (**B**), and calculations for 10 K in **(C)**. The blue circles, red triangles, and red circles in (**B**) are extracted from Fig. 2C, while those in (**C**) are from fig. S6B. The blue triangles correspond to the qFM mode of Fe^{3+}, obtained from separate experiments with a 90° rotated incident THz magnetic field polarization. The vertical error bars indicate a frequency resolution determined by the time window (Δf = 1/30 ps = 0.0333 THz for the qFM mode and Δf = 1/35 ps = 0.0286 THz for all other modes). The horizontal error bar indicates a standard deviation.

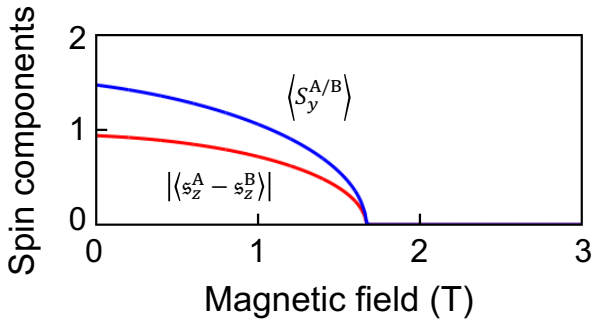

Figure S11: **Two order parameters evidencing the magnonic SRPT calculated at 2 K in the presence of the magnetic field.**

Table S1: **Mean-field model parameters from fitting and Ref. (*21*).** Listed parameter uncertainties are errors of fit, determined by the method in Ref. (*55*).

Fe^{3+} subsystem	Er^{3+} subsystem	Fe^{3+}–Er^{3+} interaction
$J_{Fe} = 4.96$ meV	$J_{Er} = 0.01328(5)$ meV	$J = 0.6$ meV
$D^y_{Fe} = -0.107$ meV	$A^x_{Er} = 0.124(4)$ meV	$D_x = 0.034$ meV
$A^x_{Fe} = 0.0073$ meV	$A^z_{Er} = 0.1480(3)$ meV	$D_y = 0.003$ meV
$A^z_{Fe} = 0.0176(3)$ meV	$A^{xz}_{Er} = 0$ meV	
$A^{xz}_{Fe} = 0$ meV	$\mathfrak{g}^x_{Er} = 4.16(8)$	
$\mathfrak{g}^x_{Fe} = 3.5734(3)$	$\mathfrak{g}^y_{Er} = 3.4$	
$\mathfrak{g}^y_{Fe} = 2$	$\mathfrak{g}^z_{Er} = 9.6$	
$\mathfrak{g}^z_{Fe} = 0.6$		

REFERENCES AND NOTES

1. R. H. Dicke, Coherence in spontaneous radiation processes. *Phys. Rev.* **93**, 99–110 (1954).

2. B. M. Garraway, The Dicke model in quantum optics: Dicke model revisited. *Philos. Transact. A Math. Phys. Eng. Sci.*. **369**, 1137–1155 (2011).

3. P. Forn-Díaz, L. Lamata, E. Rico, J. Kono, E. Solano, Ultrastrong coupling regimes of light-matter interaction. *Rev. Mod. Phys.* **91**, 025005 (2019).

4. A. Frisk Kockum, A. Miranowicz, S. De Liberato, S. Savasta, F. Nori, Ultrastrong coupling between light and matter. *Nat. Rev. Phys.* **1**, 19–40 (2019).

5. K. Cong, Q. Zhang, Y. Wang, G. T. Noe, A. Belyanin, J. Kono, Dicke superradiance in solids. *J. Opt. Soc. Am. B* **33**, C80–C101 (2016).

6. N. Marquez Peraca, A. Baydin, W. Gao, M. Bamba, J. Kono, "Ultrastrong light-matter coupling in semiconductors" in *Semiconductor Quantum Science and Technology*, M. Kira, S. T. Cundiff, Eds. (Elsevier, 2020), vol. **105**, pp. 89–151.

7. F. Schlawin, D. M. Kennes, M. A. Sentef, Cavity quantum materials. *Appl. Phys. Rev.* **9**, 011312 (2022).

8. V. Buzžek, M. Orszag, M. Rosško, Instability and entanglement of the ground state of the Dicke model. *Phys. Rev. Lett.* **94**, 163601 (2005).

9. K. Hepp, E. H. Lieb, On the superradiant phase transition for molecules in a quantized radiation field: The Dicke maser model. *Ann. Phys.* **76**, 360–404 (1973).

10. Y. K. Wang, F. T. Hioe, Phase transition in the Dicke model of superradiance. *Phys. Rev. A* **7**, 831–836 (1973).

11. D. S. Shapiro, W. V. Pogosov, Y. E. Lozovik, Universal fluctuations and squeezing in a generalized Dicke model near the superradiant phase transition. *Phys. Rev. A* **102**, 023703 (2020).

12. P. Nataf, C. Ciuti, No-go theorem for superradiant quantum phase transitions in cavity QED and counter-example in Circuit QED. *Nat. Commun.* **1**, 72 (2010).

13. M. Bamba, K. Inomata, Y. Nakamura, Superradiant phase transition in a superconducting circuit in thermal equilibrium. *Phys. Rev. Lett.* **117**, 173601 (2016).

14. P. Kirton, M. M. Roses, J. Keeling, E. G. Dalla Torre, Introduction to the Dicke model: From equilibrium to nonequilibrium, and *vice versa*. *Adv. Quantum Technol.* **2**, 1800043 (2019).

15. L. Garziano, A. Settineri, O. Di Stefano, S. Savasta, F. Nori, Gauge invariance of the Dicke and Hopfield models. *Phys. Rev. A* **102**, 023718 (2020).

16. D. Lamberto, O. D. Stefano, S. Hughes, F. Nori, S. Savasta, Quantum phase transitions in many-dipole light-matter systems. arXiv:2405.10711 (2024).

17. D. Lamberto, G. Orlando, S. Savasta, Superradiant quantum phase transition in open systems: System-bath interaction at the critical point. arXiv:2411.16514 (2024).

18. K. Rzażewski, K. Wódkiewicz, W. Żakowicz, Phase transitions, two-level atoms, and the A^2 term. *Phys. Rev. Lett.* **35**, 432–434 (1975).

19. G. M. Andolina, F. M. D. Pellegrino, V. Giovannetti, A. H. MacDonald, M. Polini, Cavity quantum electrodynamics of strongly correlated electron systems: A no-go theorem for photon condensation. *Phys. Rev. B* **100**, 121109 (2019).

20. P. Nataf, T. Champel, G. Blatter, D. M. Basko, Rashba cavity QED: A route towards the superradiant quantum phase transition. *Phys. Rev. Lett.* **123**, 207402 (2019).

21. M. Bamba, X. Li, N. Marquez Peraca, J. Kono, Magnonic superradiant phase transition. *Commun. Phys.* **5**, 3 (2022).

22. X. Li, M. Bamba, Q. Zhang, S. Fallahi, G. C. Gardner, W. Gao, M. Lou, K. Yoshioka, M. J. Manfra, J. Kono, Vacuum Bloch–Siegert shift in Landau polaritons with ultra-high cooperativity. *Nat. Photonics* **12**, 324–329 (2018).

23. S. Hughes, C. Gustin, F. Nori, Reconciling quantum and classical spectral theories of ultrastrong coupling: Role of cavity bath coupling and gauge corrections. *Opt. Quantum* **2**, 133–139 (2024).

24. X. Li, M. Bamba, N. Yuan, Q. Zhang, Y. Zhao, M. Xiang, K. Xu, Z. Jin, W. Ren, G. Ma, S. Cao, D. Turchinovich, J. Kono, Observation of Dicke cooperativity in magnetic interactions. *Science* **361**, 794–797 (2018).

25. N. Marquez Peraca, X. Li, J. M. Moya, K. Hayashida, D. Kim, X. Ma, K. J. Neubauer, D. F. Padilla, C. L. Huang, P. Dai, A. H. Nevidomskyy, H. Pu, E. Morosan, S. Cao, M. Bamba, J. Kono, Quantum simulation of an extended Dicke model with a magnetic solid. *Commun. Mater.* **5**, 42 (2024).

26. T. Makihara, K. Hayashida, G. T. Noe II, X. Li, N. Marquez Peraca, X. Ma, Z. Jin, W. Ren, G. Ma, I. Katayama, J. Takeda, H. Nojiri, D. Turchinovich, S. Cao, M. Bamba, J. Kono, Ultrastrong magnon–magnon coupling dominated by antiresonant interactions. *Nat. Commun.* **12**, 3115 (2021).

27. K. Hayashida, T. Makihara, N. Marquez Peraca, D. Fallas Padilla, H. Pu, J. Kono, M. Bamba, Perfect intrinsic squeezing at the superradiant phase transition critical point. *Sci. Rep.* **13**, 2526 (2023).

28. J. M. Lee, H.-W. Lee, M.-J. Hwang, Cavity magnonics with easy-axis ferromagnets: Critically enhanced magnon squeezing and light-matter interaction. *Phys. Rev. B* **108**, L241404 (2023).

29. H. Yuan, Y. Cao, A. Kamra, R. A. Duine, P. Yan, Quantum magnonics: When magnon spintronics meets quantum information science. *Phys. Rep.* **965**, 1–74 (2022).

30. L. Liensberger, A. Kamra, H. Maier-Flaig, S. Geprägs, A. Erb, S. T. B. Goennenwein, R. Gross, W. Belzig, H. Huebl, M. Weiler, Exchange-enhanced ultrastrong magnon-magnon coupling in a compensated ferrimagnet. *Phys. Rev. Lett.* **123**, 117204 (2019).

31. A. Kamra, W. Belzig, A. Brataas, Magnon-squeezing as a niche of quantum magnonics. *Appl. Phys. Lett.* **117**, 090501 (2020).

32. C. Emary, T. Brandes, Quantum chaos triggered by precursors of a quantum phase transition: The Dicke model. *Phys. Rev. Lett.* **90**, 044101 (2003).

33. X. Li, D. Kim, Y. Liu, J. Kono, Terahertz spin dynamics in rare-earth orthoferrites. *Photon. Insights* **1**, R05 (2022).

34. G. Herrmann, Resonance and high frequency susceptibility in canted antiferromagnetic substances. *J. Phys. Chem. Solid* **24**, 597–606 (1963).

35. V. Klochan, N. Kovtun, V. Khmara, Low-temperature spin configuration of iron ions in erbium orthoferrite. *Sov. Phys. JETP* **41**, 357 (1975).

36. M. P. Zic, W. T. Fuhrman, K. Wang, S. Ran, J. Paglione, N. P. Butch, Coupled spin waves and crystalline electric field levels in candidate multiferroic $ErFeO_3$. *J. Appl. Phys.* **130**, 014102 (2021).

37. R. L. White, Review of recent work on the magnetic and spectroscopic properties of the rare-earth orthoferrites. *J. Appl. Phys.* **40**, 1061–1069 (1969).

38. A. M. Kadomtseva, I. B. Krynetskiĭ, V. M. Matveev, Nature of the spontaneous and field-induced low-temperature orientational transitions in erbium orthoferrite. *J. Exp. Theor. Phys.* **52**, 732–737 (1980).

39. I. M. Vitebskiĭ, N. K. Danshin, A. I. Izotov, M. A. Sdvizhkov, L. T. Tsymbal, Anomalous critical dynamics of a low-temperature transition in erbium orthoferrite. *J. Exp. Theor. Phys.* **71**, 187–190 (1990).

40. A. Baydin, T. Makihara, N. M. Peraca, J. Kono, Time-domain terahertz spectroscopy in high magnetic fields. *Front. Optoelectron.* **14**, 110–129 (2021).

41. G. F. Herrmann, Magnetic resonances and susceptibility in orthoferrites. *Phys. Rev.* **133**, A1334 (1964).

42. K. Yamaguchi, T. Kurihara, Y. Minami, M. Nakajima, T. Suemoto, Terahertz time-domain observation of spin reorientation in orthoferrite $ErFeO_3$ through magnetic free induction decay. *Phys. Rev. Lett.* **110**, 137204 (2013).

43. V. G. Baryakhtar, I. M. Vitebeskiĭ, D. A. Yablonskiĭ, Theory of metamagnetic phase transitions. *Sov. Phys. Solid State* **19**, 1249–1254 (1977).

44. N. K. Danshin, V. N. Derkachenko, N. M. Kovtun, M. A. Sdvizhkov, Metamagnetic phase transition in $ErFeO_3$. *Sov. Phys. Solid State* **28**, 1461–1464 (1986).

45. D. L. Wood, L. M. Holmes, J. P. Remeika, Exchange fields and optical Zeeman effect in $ErFeO_3$. *Phys. Rev.* **185**, 689–695 (1969).

46. A. K. Zvezdin, A. A. Muchin, A. I. Popov, Magnetic-structure instability resulting from the intersection of energy levels. *JETP Lett.* **23**, 240 (1976).

47. D. Porras, P. A. Ivanov, F. Schmidt-Kaler, Quantum simulation of the cooperative Jahn-Teller transition in 1D ion crystals. *Phys. Rev. Lett.* **108**, 235701 (2012).

48. M. Hagiwara, K. Katsumata, H. Yamaguchi, M. Tokunaga, I. Yamada, M. Gross, P. Goy, A complete frequency-field chart for the antiferromagnetic resonance in MnF_2. *Int. J. Infrared and Mill.* **20**, 617–622 (1999).

49. X. X. Zhang, Z. C. Xia, Y. J. Ke, X. Q. Zhang, Z. H. Cheng, Z. W. Ouyang, J. F. Wang, S. Huang, F. Yang, Y. J. Song, G. L. Xiao, H. Deng, D. Q. Jiang, Magnetic behavior and complete high-field magnetic phase diagram of the orthoferrite $ErFeO_3$. *Phys. Rev. B* **100**, 054418 (2019).

50. K. P. Belov, A. K. Zvezdin, A. M. Kadomtseva, R. Z. Levitin, Spin-reorientation transitions in rare-earth magnets. *Sov. Phys. Usp.* **19**, 574–596 (1976).

51. A. M. Balbashov, G. V. Kozlov, A. A. Mukhin, A. S. Prokhorov, “Submillimeter spectroscopy of antiferromagnetic dielectrics: Rare-earth orthoferrites” in *High Frequency Processes in Magnetic Materials* (World Scientific Publishing, 1995), pp. 56–91.

52. V. D. Buchelnikov, N. K. Danshin, L. T. Tsymbal, V. G. Shavrov, Magnetoacoustics of rare-earth orthoferrites. *Phys Uspekhi* **39**, 547–572 (1996).

53. J. Zhang, “Microwave spectroscopy on two dimensional electron/hole gases,” thesis, Rice University, Houston, TX (2018).

54. T. E. Kritzell, A. Baydin, F. Tay, R. Rodriguez, J. Doumani, H. Nojiri, H. O. Everitt, I. Barsukov, J. Kono, Terahertz cavity magnon polaritons. *Adv. Opt. Mater.* **12**, 2302270 (2024).

55. K. W. Vugrin, L. P. Swiler, R. M. Roberts, N. J. Stucky-Mack, S. P. Sullivan, Confidence region estimation techniques for nonlinear regression in groundwater flow: Three case studies. *Water Resour. Res.* **43**, W03423 (2007).